2009

Fabrication and Device Applications of Self Assembled Nanostructures

Bhargava Ram Kanchibotla V
Virginia Commonwealth University

FABRICATION AND DEVICE APPLICATIONS OF SELF ASSEMBLED NANOSTRUCTURES

A Dissertation submitted in partial fulfillment of the requirements for the degree of Doctor of Philosophy at Virginia Commonwealth University.

by

BHARGAVA KANCHIBOTLA
M.S., Texas Technological University, 2005
M.Sc., University of Hyderabad (Andhra Pradesh, India), 2001
B.Sc., Osmania University (Andhra Pradesh, India), 1999

Director: SUPRIYO BANDYOPADHYAY
PROFESSOR, DEPARTMENT OF ELECTRICAL AND COMPUTER ENGINEERING
AND DEPARTMENT OF PHYSICS

Virginia Commonwealth University
Richmond, Virginia
May, 2009

Acknowledgement

The work described in the report would not have been possible with the constant support and encouragement of the following people and I am grateful to them and would like to thank them for all the support.

- Prof Supriyo Bandyopadhyay for giving me the opportunity to work in his group, for his invaluable support and guidance during the last four years, and also giving me the freedom to work on different projects without which none of projects would have been successful.
- National Science Foundation and (NSF-USA) and Air Force Office of Scientific Research (AFSOR-USA) for providing the financial support to carry out some of the project in this work.
- Prof Garry Tepper and his group at Department of Mechanical University, Virginia Commonwealth University for constant support and help with experiments related to one the projects in this work.
- Prof Marc Cahay and Dr Kalyan Garre at University of Cincinnati for all the encouragement and support for carrying out collaboration work.
- Prof Latika Menon at Northeastern University and Mr Deeder Aurongzeb at General Electric's for guidance and encouragement throughout the course of my graduate study here at VCU.

- All the members of my dissertation committee Dr Gary Atkinson, Dr Ramana Pidaparthi, Dr Hadis Morkoc, Dr Gary Tepper and Dr Supriyo Bandyopadhyay for agreeing to be a part of the committee.
- All the members of Quantum Device Laboratory, Wright Micro fabrication Center for support and help during the course of this work.

Table of Contents

Page

List of Figures

Page

Abstract

FABRICATION AND DEVICE APPLICATIONS OF SELF ASSEMBLED NANOSTRUCTURES

By Bhargava Kanchibotla

A Dissertation submitted in partial fulfillment of the requirements for the degree of Doctor of Philosophy at Virginia Commonwealth University.

Virginia Commonwealth University, 2009

Major Director: Supriyo Bandyopadhyay
Professor, Department of Electrical and Computer Engineering and Department of Physics

The spin dynamics of electrons in inorganic and organic semiconducting nanostructures has become an area of interest in recent years. The controlled manipulation of an electron's spin, and in particular its phase, is the primary requirement for applications in quantum information processing. The phase decoheres in a time known as the transverse relaxation time or T_2 time. We have carried out a measurement of the ensemble-averaged transverse spin relaxation time (T_2^*) in bulk and few molecules of the organic semiconductor *tris*-(*8-hydroxyquinolinolato aluminum*) or Alq_3. The Alq_3 system exhibits two characteristic T_2^* times: the longer of which is temperature independent and the shorter is temperature dependent, indicating that the latter is most likely limited by spin-phonon interaction. Based on the measured data, we infer that the single-particle T_2 time

in Alq_3 is probably long enough to meet *Knill's criterion* for fault-tolerant quantum computing even at *room temperature*. Alq_3 is also an optically active organic, and we propose a simple optical scheme for spin qubit readout. Moreover, we found that the temperature-dependent T_2^* time is considerably shorter in bulk Alq_3 powder than in few molecules confined in 1–2-nm-sized cavities. Because carriers in organic molecules are localized over individual molecules or atoms but the phonons are delocalized, we believe that this feature is caused by a phonon bottleneck effect.

Organic fluorophore molecules, electrosprayed within nanometer sized pores of an anodic alumina film, exhibit unusually large *molecule-specific* red- or blue-shifts in the fluorescence peak. This molecular specificity allows us to resolve different constituents in a mixture optically, providing a unique new technology for bio- and chemical sensing. We have also observed that the fluorescence efficiency progressively increases with decreasing pore diameter. This trend cannot be explained by the usual photo carrier confinement model since the photo carriers are localized over individual molecules (or atoms) which are much smaller than the pore diameter. A more likely explanation is the metal enhanced fluorescence caused by the plasmon resonance of nanotextured aluminum lying at the bottom of the pores.

.

CHAPTER 1. Introduction

1.1 Motivation

Nanostructures are an assembly of atoms with size ranging from ~1 to 200nm. Some examples of nanostructures are as follows: atomic clusters (0D), fine particles (0D), nanowires (1D), ultra thin films (2D), multilayer (2D), etc. [1]. Due to their low dimensionality and extremely small length scale, they often exhibit new and enhanced properties in comparison with the bulk structures. Observation of unique and interesting properties at the nanoscale, has led to the exciting possibility of utilizing these structures for information processing, magnetic recording, magnetic random access memories, miniature sensing devices, integrated magneto-electronic devices, spin based devices, and several other applications . Of the many areas of applications, quantum computing and bio and chemical sensors are of high interest. This thesis deals with the application of self assembled nanostructures in the above mentioned areas.

1.2 Quantum Computing

Historically, there has been evolution in the computer technology. During the early days of computers, the machine occupied a large volume of space. But now days, we have computers (laptop) that fit in the back pocket, thanks to the revolutionary technological development of the continued miniaturization in the microprocessor technology right from the time of invention of the transistor and the integrated circuits. As a result of the miniaturization, the process time for the computers to perform complex tasks has greatly

improved and this trend seems to continue with the further growth in this field. The day will not be far when computers will be realized at the atomic scale. This issue was noticed by the great physicist and Nobel Laurent Dr Richard Feynman in the early 80's. Ever since then, theoretical and experimental research was carried out rigorously in this exciting field termed as 'quantum computing', because at the atomic scale, matter behaves differently due to principles of quantum mechanics [2].

Now, the question is how does one perform computation at quantum level? It's well known that in case of classical computing, information is processed in 'bits' namely 0 or 1. Quantum computer does not process classical bits, but in 'qubit' which are neither 0 nor 1 but a *coherent superposition* of classical bits 0 and 1. The qubit is written as

$$qubit = \alpha|0> + \beta|1> \quad \text{.....1}$$

where |0 > denotes the state in which the qubit has a value of 0 and |1 > denotes the state in which the qubit has a value of 1[2]. The coefficient α and β are complex quantities squared magnitudes denote the probability that if a measurement is performed on the qubit, it will be found to have a value of 0 and 1 respectively. Prior to any measurement the qubit is neither 0 nor 1, but in a coherent superposition state. Since the measurement of the qubit will yield a value of either 1 or 0, the complex quantities follow the rule $|\alpha|^2 + |\beta|^2 = 1$

It is important to note that Equation (1) *does not* imply that the qubit is sometimes in state |0 > with probability $|\alpha|^2$, and the rest of the time in state |1 > with probability $|\beta|^2$. It is only after measurement that the qubit collapses to a classical bit and assumes a definite value of 0 or 1. Prior to the measurement, it *does not* have a definite value; it is

both 0 and 1, *all the time*. It is therefore called a superposition state but quantum computing depends critically on the *phase coherence* of α and β. Reference 2 gives a nice example to understand the issue of *phase coherence* which is discussed below.

Consider a (hypothetical) bit-flip operator whose action is to flip a bit from 0 to 1 and vice versa. Its action on a bit can be represented as the expected value of this operator for a system described by a qubit, we will get where θ is the phase angle difference between α and β.

The fact that $|0>$ and $|1>$ are orthogonal to each other is obvious because any measurement outcome can produce either a 0 or a 1, and absolutely nothing in between. Thus the two possible outcomes are mutually exclusive, meaning that the two states are orthogonal to each other. Equation (4) clearly shows that there are quantities that depend on the phases of a0 and a1. Thus maintaining the correct phase relations between these quantities, or "coherence" is important.

1.3 Thesis organization:

The thesis is organized as follows. Chapter 2 describes the electrochemical method used to prepare nanoporous alumina membranes. Factors that influence the process of anodization and in turn control the pore parameters are briefly discussed. Two-Step anodization process used to fabricate highly ordered nanoporous membranes is also described.

Chapter 3 deals with the measurement of the ensemble averaged transverse spin relaxation time (T_2^*) in bulk and few molecules of the organic semiconductor *tris (8−hydroxyquinolinolato aluminum)* or Alq_3. This system exhibits two characteristic T_2^*

times, the longer of which is temperature-independent and the shorter is temperature-dependent, indicating that the latter is most likely limited by spin phonon interaction. Based on the measured data, we infer that the single particle T_2 time is long enough to meet Knill's criterion for fault tolerant quantum computing, even at room temperature. Alq_3 is also an optically active organic and we propose a simple optical scheme for spin qubit read out. Moreover, we found that the temperature-dependent T_2^* time is considerably shorter in bulk Alq_3 powder than in few molecules confined in 1-2 nm sized cavities, which is suggestive of a new type of "phonon bottleneck effect". This is very intriguing for organic molecules where carriers are always localized over individual molecules but the phonons are delocalized.

Chapter 4 describes the application of nanostructures in the area of bio and chemical sensing. Here, we show that by confining organic fluorophore molecules in nanometer sized pores of an anodic alumina film with exposed nanotextured metal at the bottom, we can simultaneously increase the fluorescence intensity many fold (i.e. increase detectivity) and at the same time induce a molecule-specific red- or blue-shift the fluorescence peak which allows us to discriminate the fluorescence signal from background fluorescence (i.e. increase selectivity). The unusually large *molecule-specific* red- or blue-shifts also allow us to resolve different constituents in a mixture optically, providing a unique new technology for bio- and chemical sensing.

Chapter 5 we report the formation of hollow oxide nanostructures by oxidation of aluminum nanodots on gold thin film. The nanodots are formed by rapid thermal annealing of the thin film close to its melting point. The heights of the dots can be easily controlled via the initial thickness and temperature. The structure exhibits a

phase transition when electrochemically oxidized and forms porous structure with a stepped interior. Despite the high level of disorder, a correlation length can be easily identified from the Fourier transformation of the surface. UV–visible spectroscopy and Fourier transform infrared spectroscopy show a stop gap at 1800 cm^{-1} showing the potential for photonic material application despite the high level of disorder.

Chapter 6 we report slow correlated growth mode in energetic cluster vapor deposited organic light emissive material tris (8-hydroxyquinoline) aluminum (Alq3) from 5 nm to 100nm. Phase modulated atomic force microscopy shows very slow grain growth with thickness with very small phase differences within the film. Fractal dimension (FD) calculated from correlation function shows growth process above 10nm consistent with diffusion-limited aggregation. For low thickness (5 nm), photoluminescence measurement shows the emission peak is shifted by ~0.4 eV toward lower wavelength.

Chapter 7 we report the reduction of shorts in OLED devices using shorting reduction layer deposited sing ALD. This work is carried out as part of the internship at Eastman Kodak Company.

CHAPTER2. Self Assembled Nanostructures Using Nanoporous Alumina Membranes

2.1 Introduction

Nanotechnology, the science and engineering of nanometer sized objects, is a major research endeavor owing to the innumerable possibilities that the field has to offer, apart from being a profitable enterprise. Nanostructures exhibit unique physical and chemical properties compared to 'bulk' structures. They have important applications in developing cutting edge technology in such diverse areas as medicine, computing, communication, sensing, defense, homeland security, informatics and life sciences [3].

Fabrication or synthesis is the first step in producing nanostructures. A plethora of nanofabrication techniques has been developed in recent years, ranging from the very expensive to the inexpensive. 'Self Assembly' is a nanofabrication technique that has captured the imagination of many in the field primarily because it is easy, inexpensive, has a rapid throughput, and it often requires minimal investment in equipment and infrastructure. Self assembly is any process whereby nanostructures spontaneously nucleate or assemble in a suitable medium under the proper conditions. Depending on the medium and the external environment, the nanostructures can sometimes 'self order', meaning that they automatically arrange themselves into a regimented (usually periodic) array in space. This technique is *parallel* unlike direct write lithography, which is *serial*.

In direct writing, nanostructures are delineated serially, one at a time, leading to an unacceptably slow throughput. In self assembly, several nanostructures are produced simultaneously (in "parallel"), leading to a fast throughput. Furthermore, self assembly is usually a gentle process causing little or no processing damage to the finished nanostructures. This is usually not the case with more conventional nanofabrication techniques such as direct write lithography, or x-ray lithography, where the patterning or exposing beam (often an electron or ion beam, or x-ray) causes severe processing damage. This is particularly debilitating in the case of semiconductor nanostructures since surface states caused by the damages can pin the Fermi level in the middle of the bandgap of the semiconductor and deplete the entire structure of mobile charge carriers.

A multitude of self assembly techniques have been reported in the literature. Some of them are "physical", such as Stranski-Krastanow mode growth of quantum dots on a lattice-mismatched substrate where the nanostructures nucleate because of strain (mechanical forces). Others are "chemical" in that chemical reactions orchestrate the spontaneous nucleation of nanostructures. In this chapter, we will be concerned with a chemical technique that is rapidly emerging as the workhorse for making well-regimented quasi periodic arrays of nanostructures, of virtually any material, on arbitrary substrates. This technique utilizes nanoporous alumina membranes that have a quasi periodic array of pores with nearly uniform diameter in the sub-10 to few hundred nm range. It is produced by the anodization of aluminum in a suitable acid with a suitable voltage. Since the pores develop spontaneously because of a process known as field assisted dissolution, the template is "self assembled". Under appropriate conditions, the

pores form a nearly periodic hexagonal close packed array. Each pore is a cylinder of uniform diameter. The aspect ratio (length to diameter ratio) can be very large without causing the diameter to vary along the length. Aspect ratios of 200:1 are routinely realized in our laboratory. Pore diameter can be made to vary from 8 nm to 200 nm by changing the nature of the acid and the anodizing voltage. These pores can be *selectively* filled up with metals, semiconductors, insulators and even superconductors by using electrodeposition. That results in a vertically standing, quasi periodic array of nanowires or quantum dots of these chosen materials housed in a ceramic matrix. The finished product is a self assembled spatially ordered array of nanostructures.

2.2 Nanoporous alumina membranes

Anodized Aluminum Oxide (alumina) nanoporous membranes have been a subject of considerable interest for a long time and detailed studies have been undertaken for more than half a century. Since the early 1990's several techniques to fabricate these membranes were developed. Their salient features are: (i) highly ordered arrays of pores, (ii) pore diameter can be controllably varied from 8 nm to few hundred nm, and (iii) pore density ranges from 10^{10}-10^{12} pores /cm^2. These membranes are a convenient template for synthesizing highly ordered, vertically standing nanowires in a ceramic matrix. The wires are electrically isolated from each other by the intervening alumina, which is an insulator. The alumina matrix can be gated with a metallic pad and a potential can be applied to this pad to lower the potential barrier between neighboring nanowires thereby introducing weak electrical coupling (tunneling). This has intriguing device applications.

Alumina is also quite effective for optical isolation since it has a relative dielectric constant between 2.5 and 3.0 at optical wavelengths**.** Nanowires embedded in alumina will act as optical waveguides if the nanowire material has a larger relative dielectric constant than what alumina has. Most semiconductors used as optical waveguides have relative dielectric constants larger than 3.0. Therefore, nanowire waveguides embedded in alumina can be effective waveguides, if the optical wavelength is comparable to, or smaller than the nanowire diameter.

2.3 Electrochemical synthesis of alumina membranes: Electropolishing of aluminum foils

Fabrication of alumina membranes with ordered array of nanopores involves several critical processes and steps. The starting material is high purity aluminum foils. We use 99.998% pure, 100 μm thick aluminum foils consisting of polycrystalline aluminum (single crystal aluminum is considerably more expensive). Square coupons of area 1 inch x 1 inch are cut of the aluminum foils for ease of handling. Surface condition of the aluminum foil is an important factor that affects the ordering of the pores and uniformity of the pore diameter. The surface roughness of Al foils, purchased off the shelf, is typically of the order of a few μm. In order to reduce that to a few tens of nanometers, we first degrease the coupons in acetone and then electropolish them in a Leeco electrolyte consisting of a solution of perchloric acid, butyl cellusolve, ethanol and distilled water for ~ 10 seconds using 45 V dc. Electropolishing creates a shiny, mirror like surface. Closer inspection (using atomic force microscopy) has revealed that electropolishing actually creates intriguing patterns on the surface of the aluminum. Depending on the voltage and duration of electropolishing, periodic ridges (with heights

of a few nm) can be produced on the Al surface. The chemical dynamics governing this process is quite complex and has been explored in detail in a number of publications. In this chapter, we will not dwell on this aspect since these patterns, while highly interesting from the perspective of basic chemical reactions and kinetics, have no major device applications.

Some groups have investigated the effect of polycrystallinity of the aluminum foil on the regularity of pore formation. The pores form a nearly periodic hexagonal close packed array, but only within a domain of size ~ few μm. There are some reports that the domain size can be increased if the foils are annealed prior to electropolishing to increase the grain size in the polycrystalline film. It is not clear if there is any correlation between the grain size and the domain size. To date, there is no widespread consensus about this matter and it remains an open question.

In our group, electropolishing is carried out in an Electromet-4 (Buehler Ltd) electro polisher, with the Al foil placed at the anode, in physical contact with the Leeco electrolyte that acts as the etchant for electropolishing. The most commonly used Leeco electrolyte is the L1 electrolyte, comprising 93 cc perchloric acid, 150 cc butyl cellusolve, 1050 cc ethyl alcohol and 205 cc distilled water. The perchloric acid is the etchant for aluminum, while ethanol and butyl cellusolve are polarizable molecules that sheath regions (crests) on the surface, which have the highest electric fields. As a result, troughs on the surface dissolve faster. This effect is counter balanced by the fact that mass transport of Al^{3+} ions from the crests is more efficient. The interplay of these two effects is responsible for the formation of ridges on the surface.

2.4 Anodization of aluminum foils

Anodization of the electropolished Al foils in a suitable acid leads to the growth of the porous alumina film on the foil surface. An electropolished Al coupon is anodized in an electrolytic cell. Fig 2.1 is the schematic diagram of the experimental step up we use to perform electrochemical anodization. The electrolytic cell is a commercial flat cell. A regulated power supply provides a highly stable DC voltage for anodization. The Aluminum foil acts as the anode and a Platinum grid is used as cathode, since it does not react with the electrolytes used for anodization. The electrolytes used are moderately strong acid (pH< 4).Typically used acids for anodization are 3% Oxalic acid, 15% Sulphuric acid and 10% Phosphoric Acid. Anodization using AC current is not feasible because anodic alumina allows current to flow in one direction only. Fig 2.2 is a top view AFM image of Al foil anodized in 3% Oxalic acid at 40 V. The darker areas are the pores and the lighter area surrounding the pores is the cell walls. The diameter of the pores is about 50nm and the interpore separation is about 100nm.

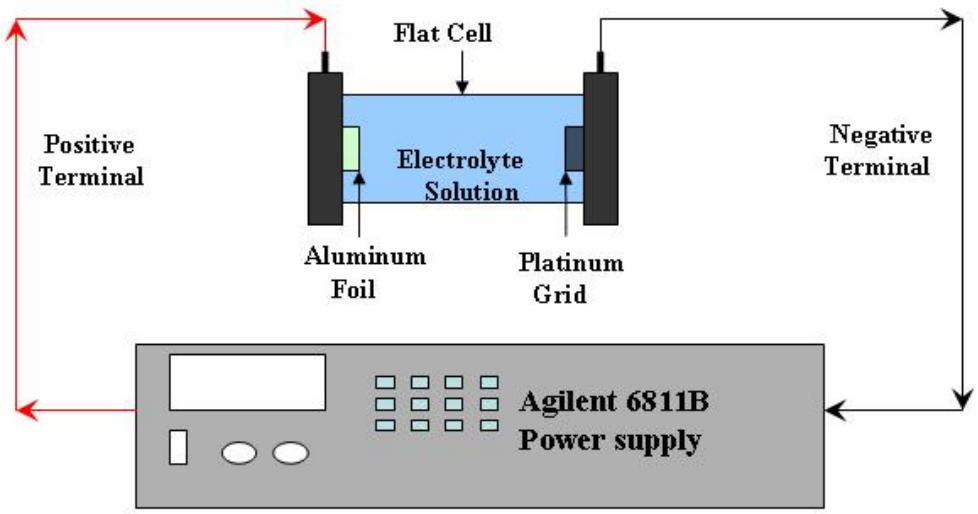

Figure 2.1 Schematic diagram of the experimental setup to perform electrochemical anodization.

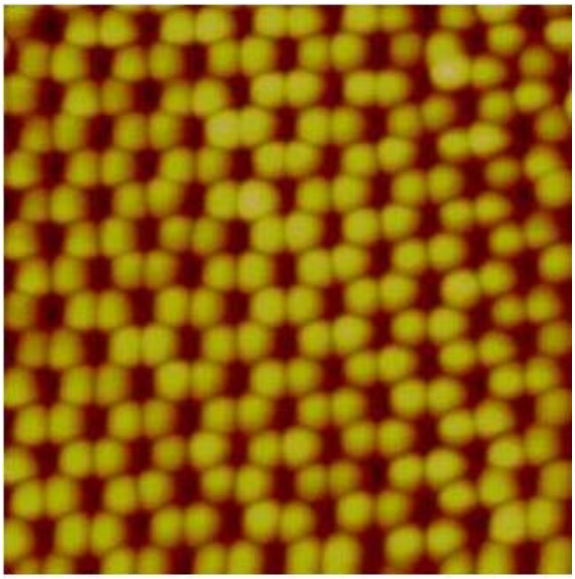

Figure 2.2 Top View Atomic Force Microscope(AFM) image of ordered pores on Al using 3% Oxalic acid at 40V DC

2.5 Growth kinetics of nanoporous alumina membranes

Many theoretical models have been proposed explaining pore growth. O'Sullivan et al[4] proposed a model based on inhomogeneous electric field distribution at pore tips and field assisted dissolution which explains why pores grow and what determines the size distribution of the pores. The pore growth is perpendicular to the surface. It was shown that parameters like the pore diameter, the interpore separation and the steady state barrier layer thickness are directly proportional to the applied voltage. Shershulsky et al [5] gave a microscopic explanation for the dependence of pore parameters on the applied voltage or the electrolyte used. Later, Jessensky et al [6] developed a model to explain densely packed hexagonal pore structure developed under special anodization conditions. The forces between the neighboring pores in the hexagonal structure are due to the mechanical stress associated with the volume expansion that occurs during the conversion of aluminum to alumina. Expansion of the material takes place only in the vertical direction because oxidation takes place over the entire pore bottom simultaneously and not all of the alumina contributes to the oxide formation since some of the Al^{3+} ions remain mobile in the oxide under the applied voltage. According to Jessensky et al, the voltage and the electrolyte composition influence the relative thickness of the porous alumina layer compared to the consumed aluminum. The most ordered pores are obtained using 0.3M solution oxalic acid at anodizing voltage of about 40V. Li et al [7], claimed that the best ordered periodic arrangements of pores are obtained when the relative volume expansion of the aluminum during oxidation is about 1.4, independent of the electrolyte. If the anodization voltage is small, the pores become

disordered as the volume of the alumina formed is smaller and the relative thickness ratio is less than 1.4. On the other hand, if the voltage is large, then the volume expansion will be too large and the ratio would be greater than 1.4. Thus producing ordered periodic pores with small or large voltages is difficult.

A typical anodization current versus time characteristic for a sample anodized in 3% oxalic acid at 40V at room temperature is shown in Fig 2.3. During the first few seconds of anodization, the current decreases rapidly until a minimum is reached. This is followed by a slow rise in the anodization current until the steady state is reached. This process is explained through a sequence of steps as shown in Fig 1.4

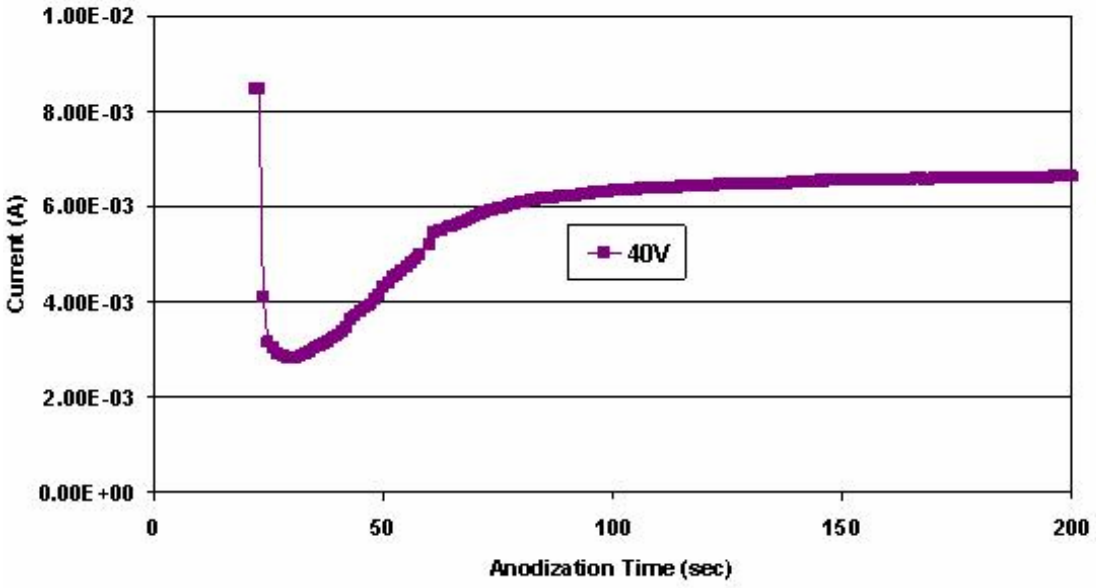

Figure 2.3 A typical anodization current versus time characteristic for a sample anodized in 3% oxalic acid at 40V at room temperature.

Initially, when the voltage is applied, an aluminum oxide layer begins to form due to oxidation of aluminum by oxygen containing ions. During this process, the anodization

current gradually drops as indicated in region A of the anodization current curve (Stage A). In the region B, fine-featured pores begin to develop, because of local dissolution of the oxide (Stage B) by hydrogen containing ions in the acid. The rate of oxidation is however, greater than the rate of oxide dissolution. Pore formation is gradually stabilized with further passage of time. This corresponds to the region C (Stage C) in the current curve. Finally, the steady state region D is reached when the pore structure stabilizes completely and the corresponding anodization current reaches a constant value (Stage D). This corresponds to the equilibrium state where the rate of oxide growth is balanced by the rate of oxide dissolution. At this stage, the pores grow perpendicular to the surface and are parallel to each other.

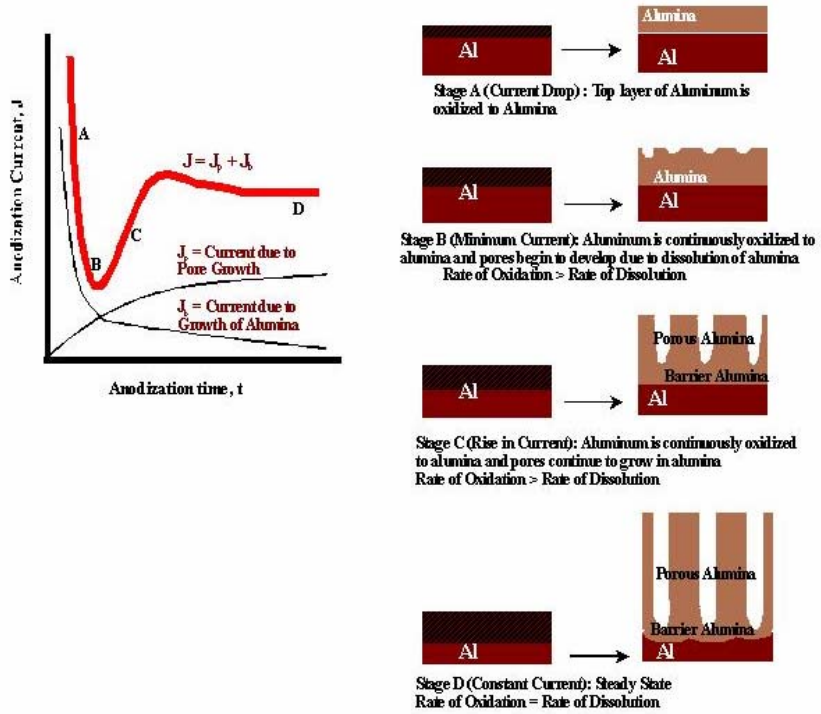

Figure 2.4 Schematic diagram of pore growth process.

The chemical reactions occurring during anodization are as follows:

At the Anode

Oxidation of Aluminum: $2Al + 3H_2O = Al_2O_3 + 6H^+ + 6e^-$

Dissolution of Alumina: $Al_2O_3 + 6H^+ = 2Al^{3+} + 3H_2O$

At the Cathode

Hydrogen Evolution: $6H^+ + 6e^- = 3H_2$

As shown by O'Sullivan et al, the growth of porous aluminum is a consequence of two competing mechanisms: oxide growth and partial dissolution of the aluminum oxide by the hydrogen ions. Oxide growth is due to the migration of oxygen containing ions O^{2-}/OH^- from the electrolyte through the oxide layer to the pore bottom and the dissolution of the oxide is due to the migration of Al^{3+} ions, which drift through the oxide layer and are ejected into the electrolyte. The net current density J can thus be thought of as being a sum of two current contributions, namely, J_b due to the growth of the barrier alumina (which decreases with time) and J_p due to pore growth (which increases with time and finally reaches a steady state as shown in Fig 2.4).

2.6 Factors controlling the self ordering of pores

The electrolyte used for anodization, the voltage applied and the duration of anodization are the key factors that are known to influence the porous structure .It has been reported in the literature that temperature of the electrolyte during anodization does influence the pore structure , but this influence is minor.

Fig 2.5 is the schematic cross section of the nanoporous structure after anodization. In the figure, the top layer is porous consisting of an array of vertical pores aligned parallel to each other. Underneath lies, the U shaped barrier layer. At the very bottom is the remaining aluminum layer left behind after anodization.

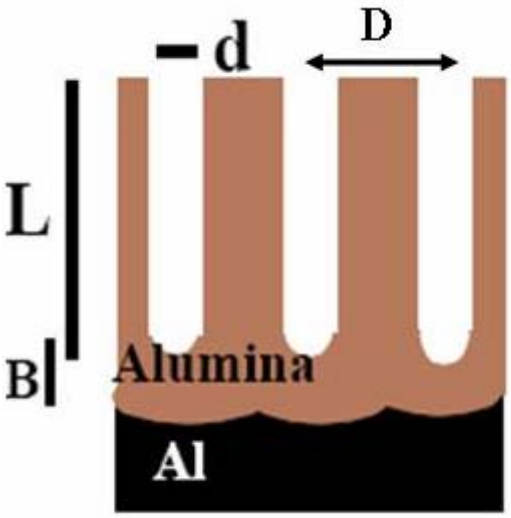

Figure 2.5 Schematic diagram of cross section of the nanoporous alumina membrane after anodization.

In the above figure, *d* is the diameter of the pore, *L* is the length of the porous membrane, and *B* is the thickness of the barrier layer, *D* is the interpore separation and *A* is the thickness of the un- reacted aluminum. Diameter of the pores, thickness of the barrier layer and the interpore separation depend on the electrolyte used and the applied voltage. The length of the pores depends on the duration of anodization and the starting thickness of the aluminum foil. Below, we discuss how these parameters are influenced by the anodization conditions.

2.7 Effect of acid strength

Weak or quasi-neutral acidic solutions (pH 5-7) are not good for anodization because they lead to the formation of flat non-porous aluminum oxide membranes, commonly called barrier-type layer or film . Anodization in a strong acid (pH< 4) results in porous aluminum oxide film. Based on the theoretical model proposed by Shershulsky et al, the pore radius varies linearly with the pH according to the relationship:

$$R_e \sim (1 + C\Phi)$$

where R_e is the pore radius, C is a constant and Φ is the pH value.

Hence, anodization using 5% phosphoric acid produces the largest pore diameter at high voltages (high pH value). Smallest pore diameter is obtained for 15% sulphuric acids since it is a strong acid (small pH value). Recently, Ono et al [8] showed self ordering porous alumina having cell diameters of 300nm and 500nm, using organic acid electrolytes such as malonic and tartaric acid solutions respectively. These acids have large pH values, yielding large pore diameters.

2.8 Effect of anodizing voltage

The DC voltage applied between the Al foil and the platinum electrode, also known as the “anodization voltage”, is a critical parameter that greatly influences the porous structure. Any arbitrary anodization voltage does not result in the formation of porous membranes. It is well known that the pore diameter and the barrier layer thickness vary with the applied voltage. The model proposed by O’Sullivan et al showed a linear relation between the pore diameter and the anodization voltage. For samples anodized in

3% oxalic acid, the optimum voltage for obtaining well ordered hexagonal pattern is about 40V, which yields a pore diameter of 50nm. The optimum anodization voltage in the case of samples anodized using 15% sulphuric acid is around 10V, and the resulting pore diameter is around 10 nm. In the case of samples anodized in 5% phosphoric acid, pore diameter as large as 350nm can be obtained using high anodization voltages, while retaining some semblance of spatial ordering. Few groups have recently reported self organization of porous alumina arrays using a mixture of acids as electrolyte . Fig 2.6 summarizes the self ordering voltages reported up till now and the corresponding pore diameters.

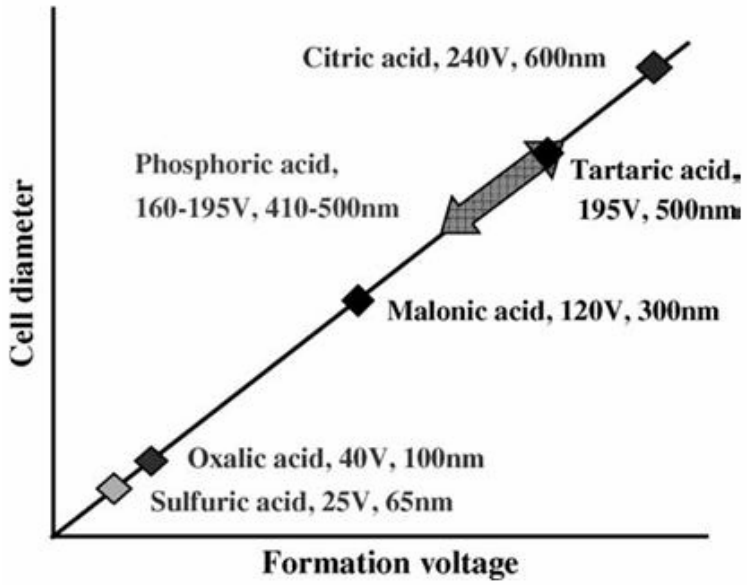

Figure 2.6 Self ordering voltages using different electrolytes and the corresponding pore diameters

The pore density varies inversely as the square of the anodizing voltage. Exponential dependence of pore density as a function of anodization voltage was reported

by Palibroda et al [9]. Al Mawlawi et al [10], showed that the pore density ρ varies with the anodization voltage V according to:

$$\rho = \frac{\alpha}{(d + \beta V)^2}$$

where α is a contant~1.15, β is a constant that depends on the acid and temperature and d is another constant. Using 3% oxalic acid, pore densities of the order 10^{10} pores/cm^2 can be obtained. Pore densities > 10^{11}pores/cm^2 can be achieved using 15% sulphuric acid. Recently, there have been some reports of the change in the porosity of anodic alumina with increasing anodization voltages. Fig 2.7 shows the porosity versus anodization voltage curve for different electrolytes. The porosity values decrease as the anodization voltage is increased, irrespective of the electrolyte used.

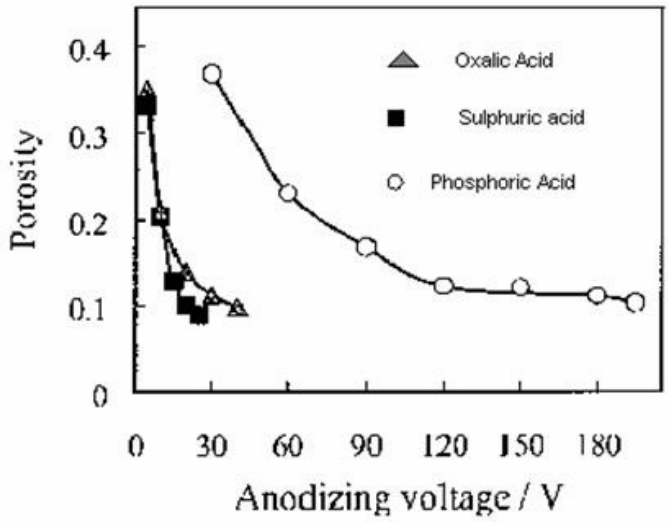

Figure 2.7 Porosity versus anodization voltage curve for different electrolytes

2.9 Effect of temperature

It has been reported in the literature that temperature affects the ordering of the pore structure but does not have any or significant influence on pore diameter or the interpore separation, when the anodization is carried out at a constant anodization voltage and electrolyte concentration . Pore structures formed at low temperatures is not as regular when compared to that formed at room temperature. The pores are found to be twisted or bent if produced at low temperatures. Sang Li et al [11] reported the effect of temperature on the ordering of the pore structure. The regularity of the pore structure was analyzed by applying fast Fourier transformation (FFT) to the SEM images.

2.10 Current density during pore growth

The values of current densities obtained during porous film growth are a key factor controlling the self ordering of pores. The pore growth mechanism based on current density was discussed in section 2.3. Recently, Ono et al reported a systematic study of pore growth in different electrolytes, focusing on the influence of current density. Fig 2.8 shows the anodization current versus time characteristics obtained for samples anodized using sulfuric acid. The anodization voltage ranges from 5V to 27V. For voltages ranging from 5V to 25V, the *I-t* curves obtained are similar to the curves discussed in section 2.3, indicating porous membrane growth. At about 27V, a high current density value was observed along with intense gas evolution at the sample surface. Interestingly, no porous growth was seen at this stage. The absence of pores at this stage is probably because the anodization voltage exceeded a certain critical value.

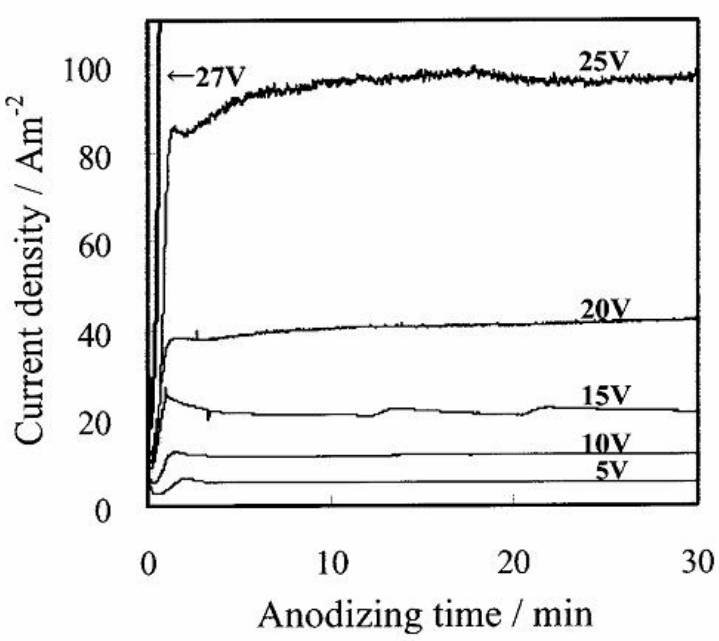

Figure 2.8 Anodization current versus time characteristics obtained for samples anodized using sulfuric acid

Similar studies were performed using oxalic and phosphoric acids. Fig 2.9 shows the anodization voltage versus current density curves for three different electrolytes. Extreme high current was observed for voltages higher than the individual self ordering voltages for the three electrolytes. It was concluded that self ordering occurs only for voltages below the individual critical voltages for the electrolytes used. Beyond the critical voltage, no film growth takes place.

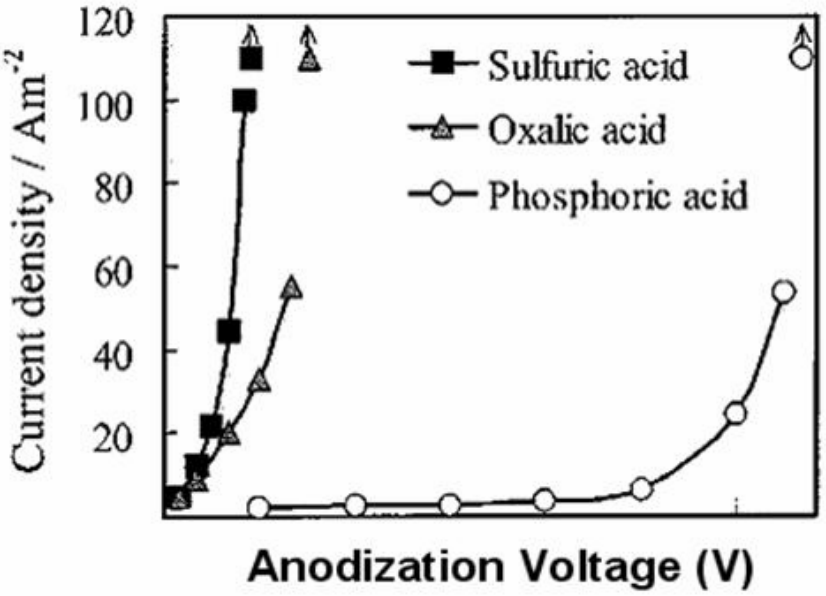

Figure 2.9 Anodization voltage versus current density curves for three different electrolytes.

2.11 Fabrication of highly ordered porous templates using multistep anodization

Porous membranes, obtained using a one-step anodization, do not contain very well ordered pores. This issue limited the use of porous templates in nanofabrication. Long range ordering is absent in these structures, even though short range ordering was present. Annealing the Al foils prior to electropolishing and anodization was suggested as a remedy, but proved unsatisfactory. The first satisfactory solution to the problem was revealed in a landmark paper published by Masuda et al [12] in 1995. They developed a technique called *multi step anodization* that significantly improved the periodicity of the pores produced in both oxalic and sulphuric acids. Highly ordered honeycomb pore structure over large areas was achieved by this technique.

Fig 2.10 is a sequence of steps that illustrates multi step anodization. First, the Al foil is electropolished and then anodized for a short time (5-10 min) which results in the formation of a thin alumina film on the surface. Now the sample is treated using a mixture of 0.2M chromic acid and 0.4M phosphoric acid in order to remove this film. Then the sample is again anodized for a long time (10 -12 hours or overnight). The long time anodization significantly reduces the number of defects and dislocations in the sample. The thickness of the film at this stage is several microns. The thick film is then etched away in a mixed acid (0.2M Chromic/0.4M Phosphoric acid) at 60^{0} C. This leaves behind a hexagonally ordered array of scallops on the surface of the aluminum.

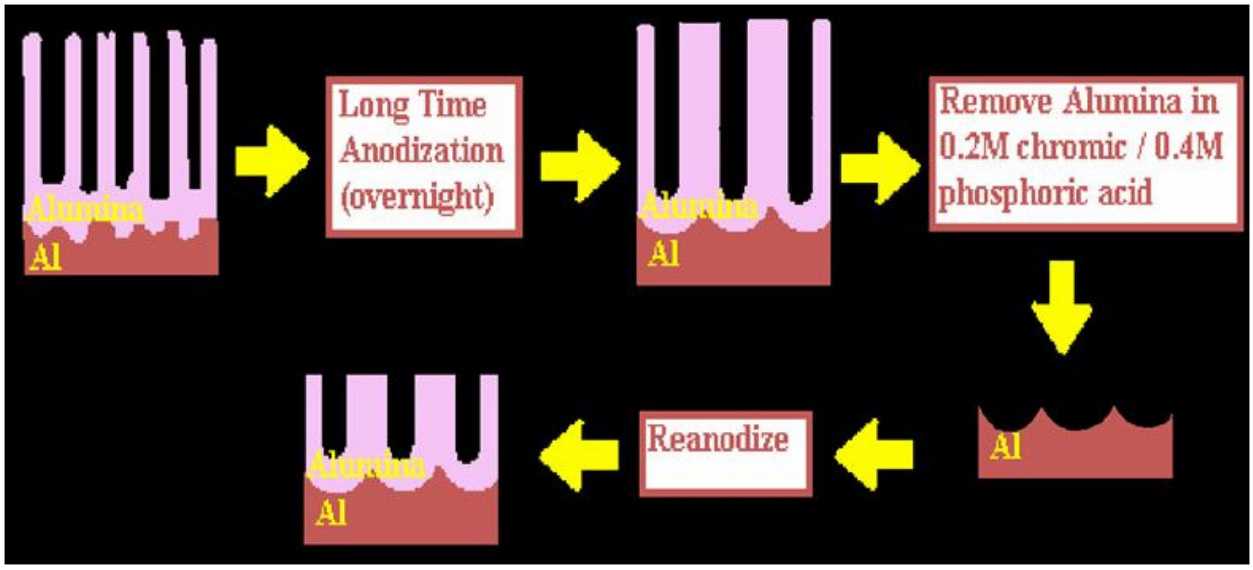

Figure 2.10 Schematic diagram showing the two step anodization process.

Fig 2.11 is the AFM image of the sample after treating with the chromic/phosphoric acid mixture. The presence of the aluminum scallops corresponds with the U shaped barrier layer at the base of the pores. The sample is then reanodized for a few minutes to acquire the

required pore length. At this stage, the ordered array of scallops acts as nucleation centers for the re-growth of the nanoporous alumina. This results in ordered pore growth.

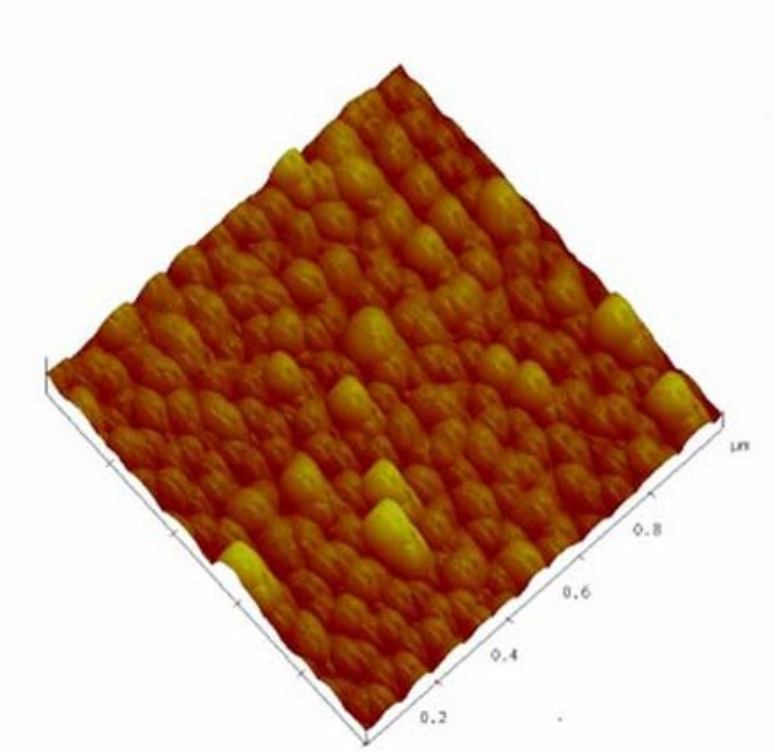

Figure 2.11 AFM image of sample after removing the porous membrane using chromic phosphoric acid

The significant improvement in the ordering of the pores can be gleaned from the images. The AFM image after the first step anodization shows the defects Fig 2.12(a). Highly ordered hexagonal structure with no defects can be seen after multi step anodization process from Fig 2.12(b). Recently, Vrublevsky et al carried out a detailed study of the growth of porous membrane during re anodization process, details of which are beyond the scope of the present work. Interested reader is referred to the article for more intricate details.

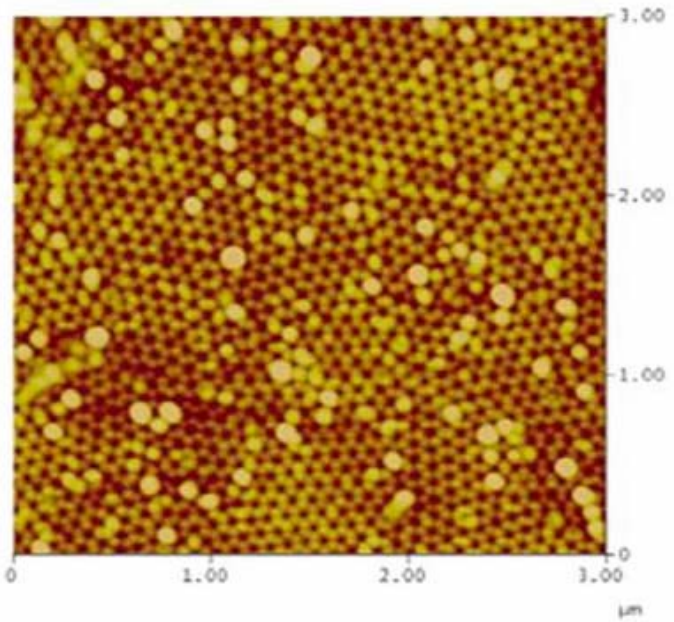

Figure 2.12a Top view AFM image of first step anodization sample using 3% oxalic acid at 40V DC.

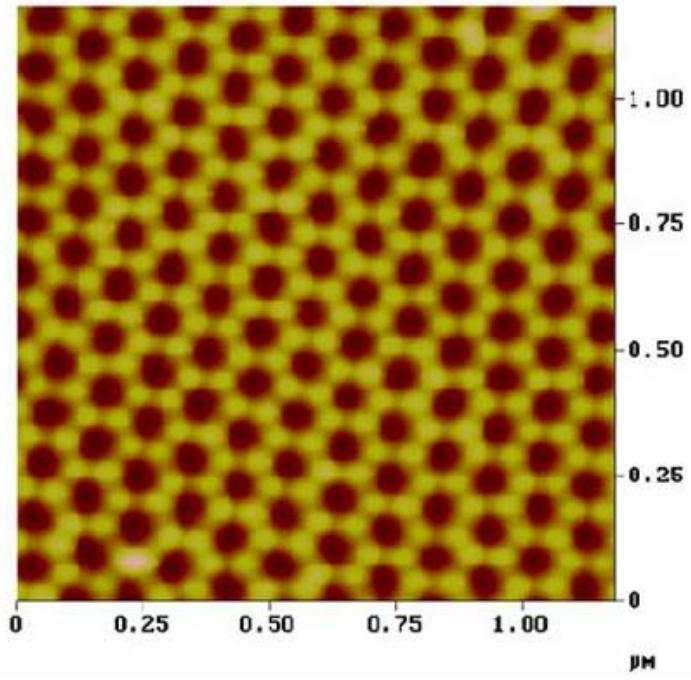

Figure 2.12b Top view AFM image of sample after two step anodization.

2.12 Techniques for removal of barrier alumina layer

The thickness of the U shaped barrier layer formed at the porous membrane and Al interface is about 10 -30 nm. This thickness depends on the electrolyte used as well as the anodization voltage. The barrier layer is a spoiler. This layer is non-conducting in nature, which prevents the passage of *conduction current* along the length of the pores, and hence DC electrodepostion of materials inside the pores is impossible unless this layer is removed. AC electrodeposition is another matter. There, atomic species are transported to within the pores via the *displacement current,* as opposed to conduction current. Since the barrier layer does not completely impede the displacement current, it is possible to selectively electrodeposit materials within the pores using AC electrodeposition, even if the barrier layer is present. However, another disadvantage of having the barrier layer is that it is hard to make electrical contacts to the materials inside the pores from the bottom since the barrier layer intervenes. Recently, techniques have been developed to either remove or thin the barrier layer.

2.13 Thinning or dissolution of barrier layer using phosphoric acid

Ansermet et al [13] developed a method for thinning the barrier layer by soaking the anodized aluminum membrane in aqueous solution of 5% Phosphoric acid for 50 minutes. This process thins the barrier layer at the pore bottom but also widens the pores since the etching in phosphoric acid is more or less isotropic. Once the barrier layer is sufficiently thinned, materials can be AC or DC electrodeposited into the porous

membrane and electrical measurements can be carried out by making contacts at the top and bottom of the membrane.

Another technique widely used to facilitate DC electrodepostion is based on complete dissolution of the barrier layer. This method can also be used to make templates for pattern transfer purposes. Fig 2.13 shows the sequence of steps describing this well known technique. First, the top layer of the porous membrane is coated with a thick organic layer to provide mechanical stability to the film. Then, the sample is treated with 3% $HgCl_2$ solution which dissolves the un-reacted Al layer from the bottom (Step C) to expose the barrier layer from the bottom. The sample is then soaked in 5% Phosphoric acid solution which removes the exposed barrier layer. The top organic layer is then etched by treating the sample with ethyl alcohol solution (Step E). After this stage, just the thin porous membrane (a "see through" film) is left behind. This delicate film can be fished out of the ethyl alcohol solution with tweezers and carefully placed on a conducting substrate for DC electrodeposition (this method calls for some operator skill since careless handling will make the film wrinkle and render it useless).

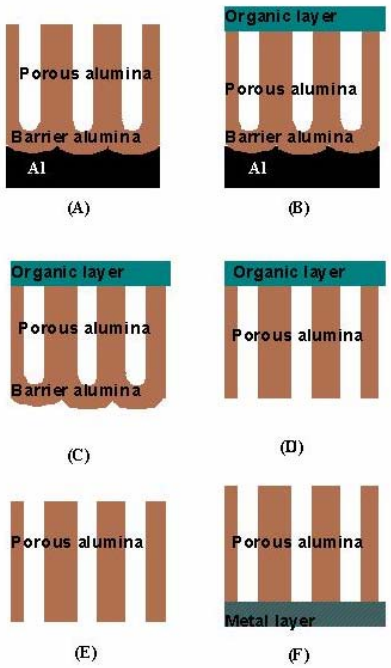

Figure 2.13 Schematic diagram of sequence of steps describing the barrier layer removal process.

2.14 Removal of barrier layer using "Reverse Polarity Etching"

In a technique developed by Rabin et al the barrier layer was etched in 5% Phosphoric acid not by mere soaking, but by applying a negative bias (negative terminal is connected to Al foil). Typically, a negative bias of 2.25 V is used. The Phosphoric acid can be replaced by a dilute solution of KCl, which has a faster etching rate. In our labs, we perform the reverse polarity etching using 1% Phosphoric acid. Fig 2.14a is the top view SEM image of a sample anodized in 3% Oxalic acid at 40 V. Fig 2.14b is the bottom view SEM image of the same sample after performing reverse polarity etching. The see-through pores can be clearly seen from this image. The “reverse bias” increases

the local concentration of the H^+ ions at the pore bottom which promotes dissolution of the barrier layer and thus opens up the pores.

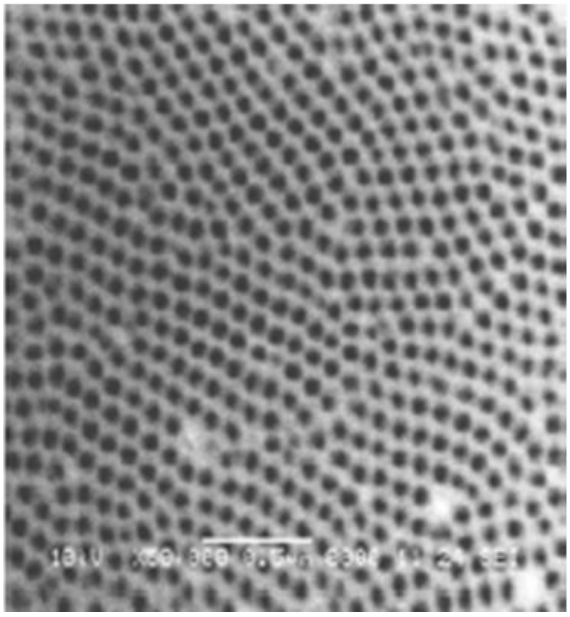

Figure 2.14a Top view SEM image of a sample anodized in 3% Oxalic acid at 40 V

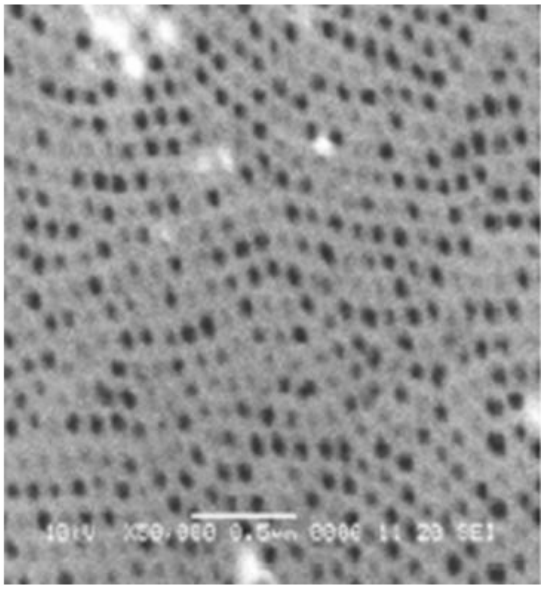

Figure 2.14b Bottom view SEM image of the sample after performing reverse polarity etching.

CHAPTER 3. Transverse Spin Relaxation times in Organic Molecules

3.1 Introduction

The π conjugated organic semiconductor Alq_3 exhibits exceptionally long longitudinal spin relaxation time T_1 (approaching 1 second at 100 K) because of weak spin-orbit inter- actions [14]. That bodes well for classical spin based devices like Spin Enhanced Organic Light Emitting Diodes [15] or classical spin based computing paradigms such as Single Spin Logic [16-17] where a long T_1 time reduces the probability of bit errors caused by unwanted spin flips. In quantum computing paradigms [18-23], the bit error probability depends on the transverse spin relaxation time T_2 rather than T_1. The probability of a spin based qubit to decohere during a qubit operation that lasts for a time duration T is roughly

$$1 - e^{\frac{-T}{T_2}}$$

Knill has shown that fault tolerant quantum computing becomes possible if this probability is less than 3% [24], i.e., if $T_2/T > 33$.

Two recent results have inspired us to look towards the Alq_3 molecule as a potential candidate for fault-tolerant spin based quantum computing. The first is the demonstration that it exhibits a long T_1 time. This result from weak spin orbit interactions

which could also make the T_2 time long enough to allow fault tolerant computing. Second, some organic molecules can be efficient quantum processors with high gate fidelity [25]. These two factors, taken together, raise the hope that Alq_3 might be a preferred platform for spin based quantum computing. This molecule also has spin-sensitive optical transitions that can be gainfully employed for spin (qubit) read out. That makes it even more attractive.

Unfortunately, it is very difficult to measure the single particle T_2 time directly in any system (including Alq_3 molecules) since it requires complicated spin echo sequences. Therefore, we have measured the ensemble averaged T_2^* time instead, since it can be ascertained easily from the line width of electron spin resonance spectrum. This time, however is orders of magnitude shorter than the actual T_2 time of an isolated spin because of additional decoherence caused by interactions between multiple spins in an ensemble [26-27]. It is particularly true of organics where spin-spin interaction is considered to be the major mechanism for spin decoherence [28]. Consequently, bulk samples (where numerous spins interact with each other) should behave differently from one or few molecules containing fewer interacting spins. In the rest of the paper, we will designate the T_2* times of bulk and few-molecule samples as T_2^b and T_2^f, respectively. We have found that they are discernibly different.

3.2 **Sample Fabrication**

In order to prepare samples containing one or few molecules, the following technique was used [29]. We first produced a porous alumina film with 10-nm pores by

anodizing commercially purchased high purity aluminum foil in 15% sulfuric acid [30]. A two-step anodizing process was employed to improve the regimentation of the pores. These porous films were then soaked in 1,2-dichloroethane ($C_2H_4Cl_2$) solution of Alq_3 for over 24 hours to impregnate the pores with Alq_3 molecules. The films were subsequently washed several times in pure $C_2H_4Cl_2$ to remove excess Alq_3. There are cracks of size 1-2 nm in the anodic alumina film produced in sulfuric acid [31-33]. In Fig. 3.1, we show a cross-section transmission electron micrograph of such a crack of width 1-2 nm.

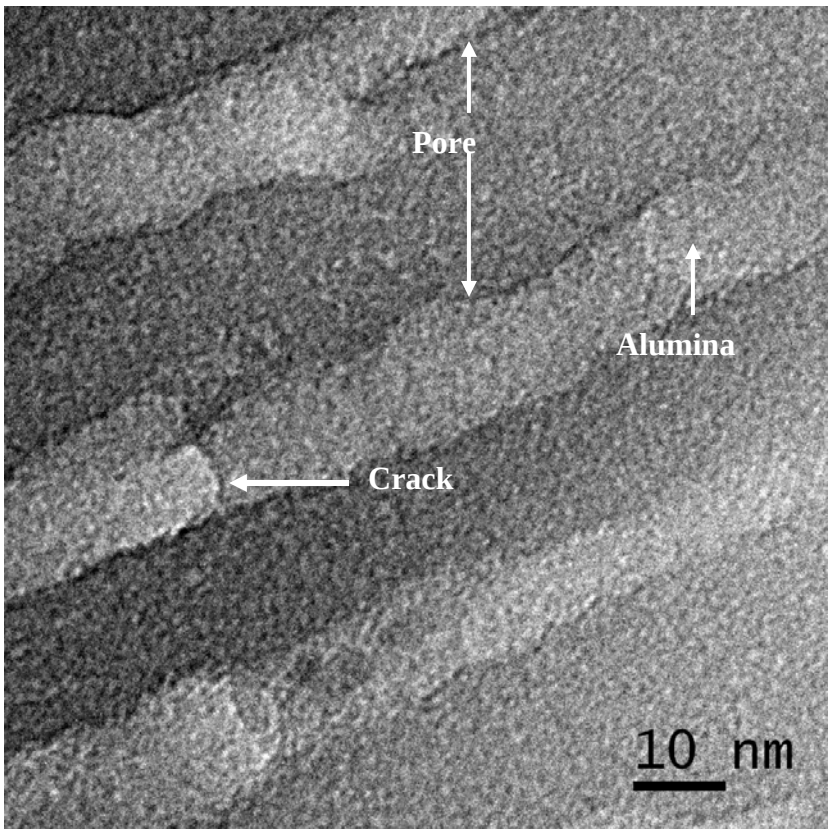

Figure 3.1 Cross-section transmission electron micrograph of porous alumina matrix. A nanovoid of diameter 1-2 nm is shown.

Ref. [33] claims that when the anodic alumina film is soaked in Alq_3 solution, Alq_3 molecules of 0.8 nm size diffuse into the cracks and come to rest in nanovoids

nestled within the cracks. Each nano-void can contain 1-2 molecules because of their size. Surplus molecules, not in the nanovoids, will be removed by repeated rinsing in $C_2H_4Cl_2$. The nanovoids are sufficiently far from each other that interaction between them is negligible. Therefore, using this fabrication technique, we will be confining one or two isolated molecules in nanovoids and measuring their T_2^f times. In contrast, the T_2^b times are measured in bulk Alq_3 powder containing a very large number of interacting molecules.

3.3 Results and Discussion

The T_2^f and T_2^b times were measured using high end electron spin resonance (ESR) spectroscopy purchased from Bruker Biospin Corporation. It is well known that Alq_3 has two spin resonances corresponding to Land´e g-factors of approximately 2 and 4 [34]. Ref. [34] determined from the temperature dependence of the ESR intensity that the g = 4 resonance is associated with localized spins in Alq_3 (perhaps attached to an impurity or defect site) while the g = 2 resonance is associated with quasi-free (delocalized) spins. From the measured line widths of these two resonances, we can estimate the T_2^f and T_2^b times for each resonance individually using the standard formula

$$T_2^f \; or \; T_2^b = \frac{1}{r_e\left(\frac{g}{2}\right)\sqrt{3}\Delta B_{pp}}$$

where r_e is a constant = 1.76 x 107$(G - s)^{-1}$, g is the Land´e g-factor and ΔB_{pp} is the full-width-at-half-maximum of the ESR line shape (the line width). We checked that the line shape is almost strictly Lorentzian, so that the above formula can be applied with

confidence[35]. Fig. 3.2 shows a typical magnetic field derivative of the ESR spectrum obtained at a temperature of 10 K corresponding to g = 2 resonance. There are three curves in this figure corresponding to the blank alumina host, bulk Alq_3 powder, and Alq_3 in 1-2 nm voids. The alumina host has an ESR peak at g = 2 (possibly due to oxygen vacancies) [36], but it is much weaker than the resonance signals from Alq_3 and hence can be easily separated. Note that the g-factor of the isolated Alq_3 molecules in nanovoids is slightly larger than that of bulk powder since the resonance occurs at a slightly higher magnetic field. More importantly, the bulk powder has a broader line width than the few molecules confined in the nanovoids. This is a manifestation of the fact that stronger spin-spin interactions in the bulk powder reduce the effective T_2^* time, i.e., $T_2^b < T_2^f$.

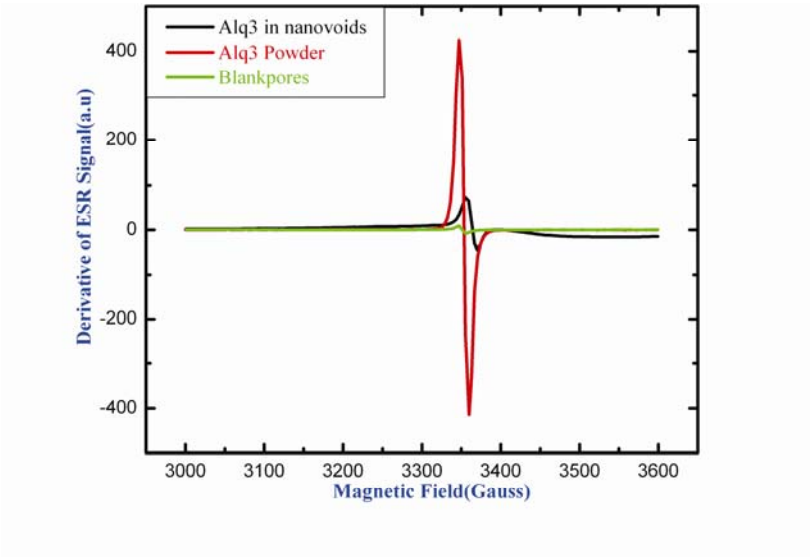

Figure 3.2 First derivative in magnetic field of the electron spin resonance spectrum corresponding to $g = 2$. The three curves are the data for the blank alumina matrix, the Alq_3 powder and Alq_3 molecules in nanovoids. The temperature is 10 K.

In Fig. 3.3, we plot the measured T_2^f and T_2^b times (associated with the resonance corresponding to g = 2) as functions of temperature from 4.2 K to 300 K. The inequality $T_2^b < T_2^f$ is always satisfied except at one anomalous data point at 4.2 K. There are two important points to note here. First, both T_2^f and T_2^b are relatively temperature independent over the entire range from 4.2 K to 300 K. This indicates that spin-phonon interactions do not play a significant role in spin dephasing. Second, both T_2^f and T_2^b times are quite long, longer than 3 nanoseconds, even at room temperature. In Fig. 3.4 we plot the measured T_2^f and T_2^b times as functions of temperature corresponding to the g = 4 resonance. The T_2^f time is plotted from 4.2 K to 300 K, but the T_2^b time in bulk powder can only be plotted up to a temperature of 100 K. Beyond that, the intensity of the ESR signal fades below the detection limit of our equipment.

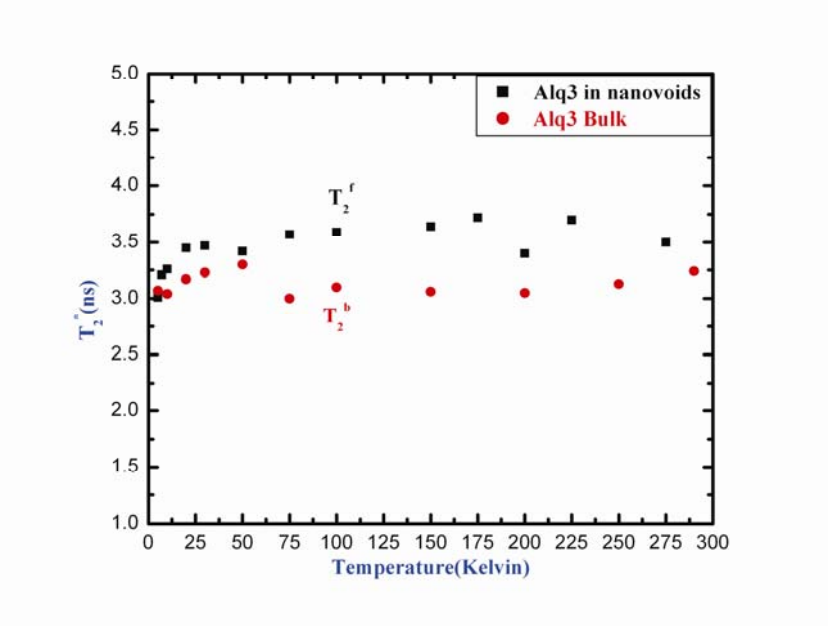

Figure 3.3 Transverse spin relaxation times as a function of temperature for $g = 2$ resonance. The two plots are for bulk *Alq₃* powder (T_2^b) and few *Alq₃* molecules (T_2^f) in nanovoids.

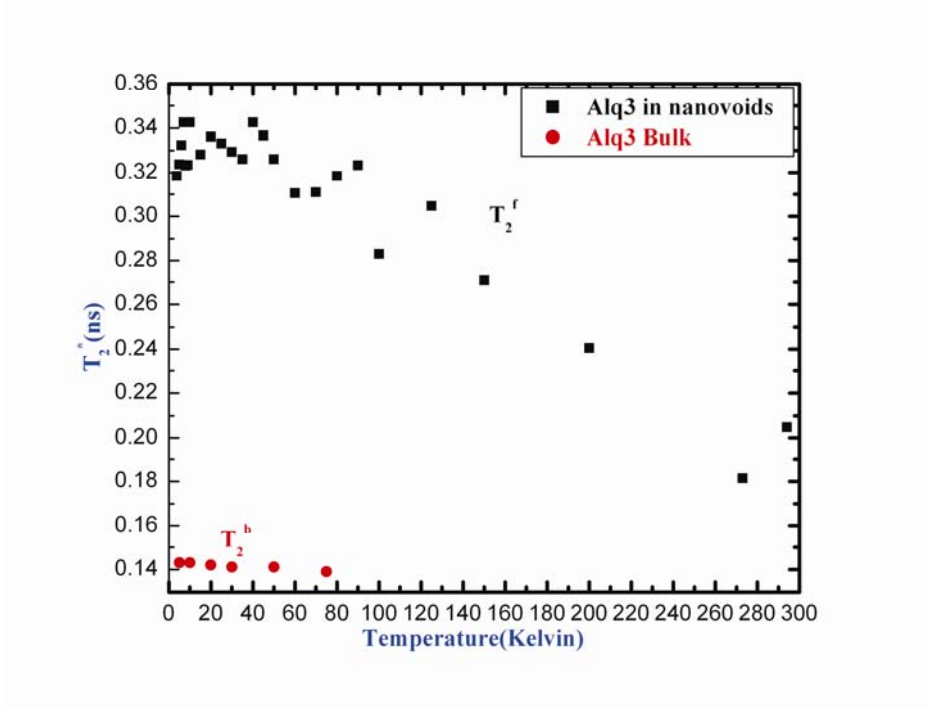

Figure 3.4 Transverse spin relaxation times as a function of temperature for $g = 4$ resonance. The two plots are for bulk *Alq₃* powder (T_2^b) and few *Alq₃* molecules (T_2^f) in nanovoids

The features to note here are that: (1) T_2^f and T_2^b are no longer temperature independent unlike in the case of the g = 2 resonance. T_2^f decreases monotonically with increasing temperature and falls by a factor of 1.7 between 4.2 K and 300 K, (2) $T_2^b < T_2^f$ and the ratio T_2^f / T_2^b decreases with increasing temperature. The maximum value of the ratio T_2^f / T_2^b is 2.4, occurring at the lowest measurement temperature of 4.2 K, and (3) both T_2^f and T_2^b times are about an order of magnitude shorter for the g = 4 resonance compared to the g = 2 resonance. The strong temperature dependence of T_2^f and T_2^b tells us that for g = 4 resonance, spin-phonon coupling plays the dominant role in spin dephasing instead of spin-spin interaction.

The spin-phonon coupling is absent or significantly suppressed for the g = 2 resonance, which is why T_2^f and T_2^b are an order of magnitude longer and also temperature independent for g = 2. The g = 2 resonance to quasi free carrier spins in Alq_3 (whose wavefunctions are extended over an entire molecule) and g = 4 resonance to localized spins (whose wavefunctions are localized over an impurity atom). If that is the case, then it is likely that the localized spins and the delocalized spins will have very different couplings to phonons since their wavefunctions are very different.

An interesting question is why should T_2^f be so much longer than T_2^b for the g = 4 resonance. The bulk has many more interacting spins than the few-molecule sample has, but if spin-spin interaction is overshadowed by spin-phonon coupling, then this should not make any difference. We believe that what is causing this behavior is a new type of phonon- bottleneck effect. For g = 4 resonance, we know that the primary dephasing agents are phonons. So what makes the spin-phonon coupling so much stronger in bulk than in nanovoids? In bulk Alq_3 powder, the phonons are not confined and form a continuum.

However, in isolated nanovoids (cavities) of ~ 2 nm diameter, the phonons are confined so that only discrete phonon modes are allowed. Any dephasing transition will then have to emit or absorb a subset of these allowed phonon modes. This reduces the transition probability considerably since few phonons are available to satisfy the energy and momentum conservations for phonon emission and absorption. This is a new type of phonon bottleneck effect, slightly different from the one discussed in ref.[37], which required carrier confinement more than phonon confinement. This new type of phonon

bottleneck effect would explain why $T_2^f > T_2^b$ when phonons are the primary dephasing agents. The bottleneck will be more severe at lower temperatures since fewer phonon modes will be occupied (Bose Einstein statistics), which is exactly what we observe. If this explanation is true, it will be the first observation of this effect in organic molecules. What makes it more intriguing is the fact that there is no quantum confinement effect on electrons since their wavefunction is at best extended over a single molecule which is only ~ 0.8 nm in size, but the phonon modes are extended over many molecules and therefore do suffer quantum confinement if the confining space is a nanovoid of ~ 2 nm in diameter. We raise the specter of phonon bottleneck only as a possibility, but cannot confirm it experimentally beyond all reasonable doubt since that would require showing progressive suppression of dephasing with decreasing nanovoid size, something that is experimentally not accessible. Nonetheless, we believe that there is a preponderance of evidence for the phonon bottleneck effect.

3.4 Conclusion

We conclude by discussing the suitability of Alq_3 molecules for quantum computing applications. For a single isolated spin in Alq_3, T_2 should be at least an order of magnitude longer than T_2^* particularly when spin-spin interaction is the major dephasing mechanism (g = 2). Since we have measured that $T_2^* \sim 3$ nanosecond at nearly all temperatures between 4.2 K and 300 K for g = 2 resonance, we expect that the single spin T_2 time will be at least 30 nanoseconds over this entire temperature range. Now, if Rabi oscillation is used for qubit operations such as rotation, then the time taken to effect

a complete spin flip is $T = h/ (2g\mu_B B_{ac})$ where g is the Land´e g-factor, μ_B is the Bohr magneton and B_{ac} is the amplitude of the ac magnetic field inducing the Rabi oscillation. With B_{ac} = 500 Gauss [38], T = 0.35 nanoseconds. Therefore, the error probability = $1 - \exp[-T/T_2] = 1.15\%$. This is less than the Knill limit of 3% for fault tolerant quantum computing, which is encouraging. We emphasize that Alq_3 does not have exceptionally long T_2 times, but it is still adequate for fault tolerant quantum computing. Nitrogen vacancy, NV^- in diamond exhibits a much longer T_2 time of several tens of microsecond at room temperature [39]. However, quantum computing paradigms based on NV − require optical gating [40-43] or cavity dark states [44] since it would be nearly impossible to place an electrical gate on top of an atomic vacancy using any of the known fabrication methods. As a result, NV − computers are not truly scalable. In contrast, the spins in Alq_3 are not bound to specific atomic sites. Instead, they extend over molecules of size ~ 1 nm, which allows electrical gating and therefore scalable renditions of quantum processors. Inorganic semiconductor qubit hosts, that will also allow electrical gating, typically have a shorter T_2^* time than Alq_3 at room temperature. Therefore, the Alq_3 system deserves due attention.

Finally, if an Alq_3 quantum dot were used as a host for a spin qubit, one would require a mechanism for reading the host spin (qubit read out). Fortunately, this can be achieved quite simply and elegantly. It is well known that only the singlet exciton recombines radiatively in Alq_3 and the triplet does not. Thus, one needs to inject a spin polarized hole into an Alq_3 quantum dot that hosts a single electron in the LUMO level, from a p-type dilute magnetic semiconductor such as GaMnAs. The hole's spin will be

known (majority spin in GaMnAs). If a photon is emitted from the Alq_3 quantum dot, then we will know that the electron's spin and the hole's spin are anti-parallel. Otherwise, they are parallel. This allows one to determine the electron's spin polarization in the Alq_3 dot (qubit read out). The optical read out mechanism requires a quantum dot photon detector to be integrated on top of the Alq_3 quantum dot hosting the spin. This is not difficult to implement and does not detract from the scalability. In conclusion, Alq_3 based quantum processors (1) are scalable, (2) are capable of fault-tolerant operation at room temperature, (3) possibly have a high degree of gate fidelity, and (4) lend themselves to an elegant qubit read out scheme. This makes them attractive candidates for quantum computers.

CHAPTER 4. Fluorescence Spectroscopy of Organic Molecules in Anodic Alumina Pores: A New Approach to Bio- and Chemical Detection*

4.1 Introduction

Detection of trace amounts of biological and chemical agents in the environment is a challenging task since the background often behaves similarly as the target agents and tends to mask their presence. This is particularly true in the case of optical detection where the fluorescence spectrum of the target species may overlap with the broad fluorescence spectrum of the background so that the target remains undetectable. A possible remedy might be to deposit a target containing sample into a suitable host that induces a large red- or blue-shift selectively in the fluorescence spectrum of the target molecules while leaving the fluorescence spectrum of the background unaffected. This will resolve the fluorescence of the target molecules and allow unambiguous optical detection. The detection capability is further enhanced if the host also increases the fluorescence efficiency of the target species selectively. In this paper, we report a series of experiments that have achieved *both* goals, i.e. inducing a molecule-specific red- or blue-shift in the fluorescence peak to improve selectivity, and simultaneously increasing the fluorescence efficiency to improve detectivity.

*This work is carried out in collaboration with Dr Gary Tepper's group , Department of Mechanical Engineering,Virginia Commonwealth University,USA

4.2 Sample Fabrication

The porous alumina films are produced by anodizing 99.999% pure amorphous Al foils in sulfuric or oxalic acid under different voltages. Prior to anodization, a foil is electropolished in a solution of perchloric acid, butyl cellusolve, ethanol and distilled water to reduce the surface roughness to less than ~ 3 nm [45-49]. Subsequent anodization produces an alumina film containing pores whose diameters depend on the acid used and the dc voltage employed during anodization. Anodization in sulfuric acid produces pores of diameter 10 nm, while anodization in oxalic acid produces pores of diameter 20 nm if the anodizing voltage is 25 V, and 50 nm if the anodizing voltage is 40 V. At the bottom of the pores, there is a "barrier layer" of alumina in contact with the aluminum substrate. Prior to electrospraying the molecules, this barrier layer is removed by a `reverse polarity etching' technique[2] that exposes the metallic aluminum at the bottom of the pores. The exposed aluminum surface assumes the shape of a pit because of the mechanical stresses created during the anodization process. Fig. 4.1 a,b and c shows an atomic force micrograph of the aluminum surface taken after dissolving out the anodic alumina film in hot chromic/phosphoric acid. The pitted landscape is clearly visible.

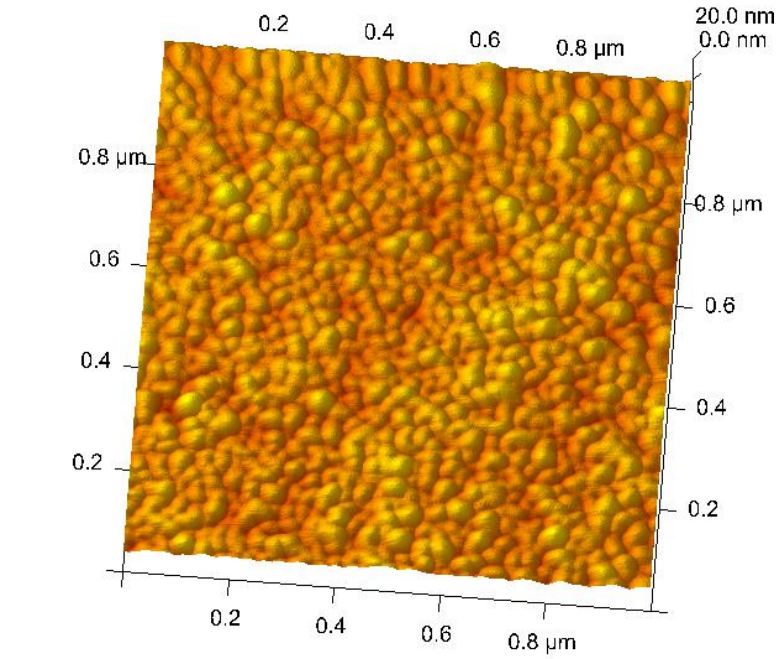
0.2
0.4
0.6
0.8 µm
20.0 nm
0.0 nm
0.8 µm
0.6
0.4
0.2
0.2
0.4
0.6
0.8 µm

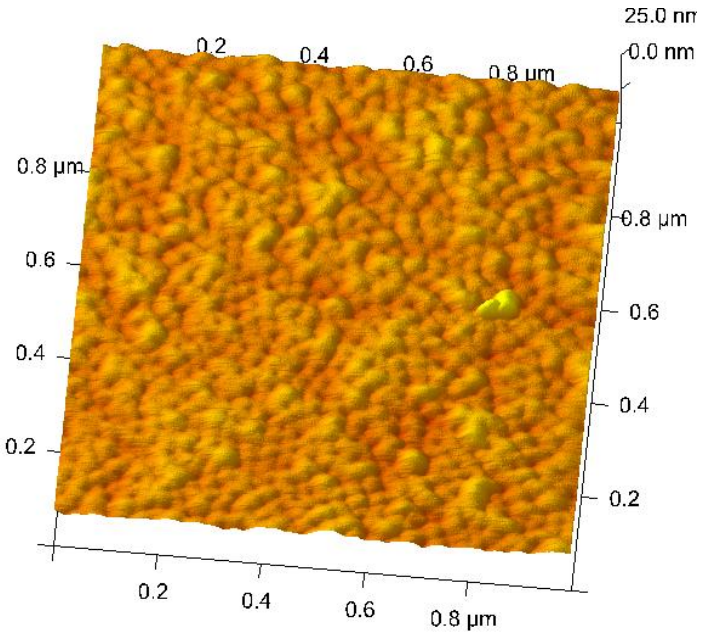
0.2
0.4
0.6
0.8 µm
25.0 nm
0.0 nm
0.8 µm
0.6
0.4
0.2
0.2
0.4
0.6
0.8 µm

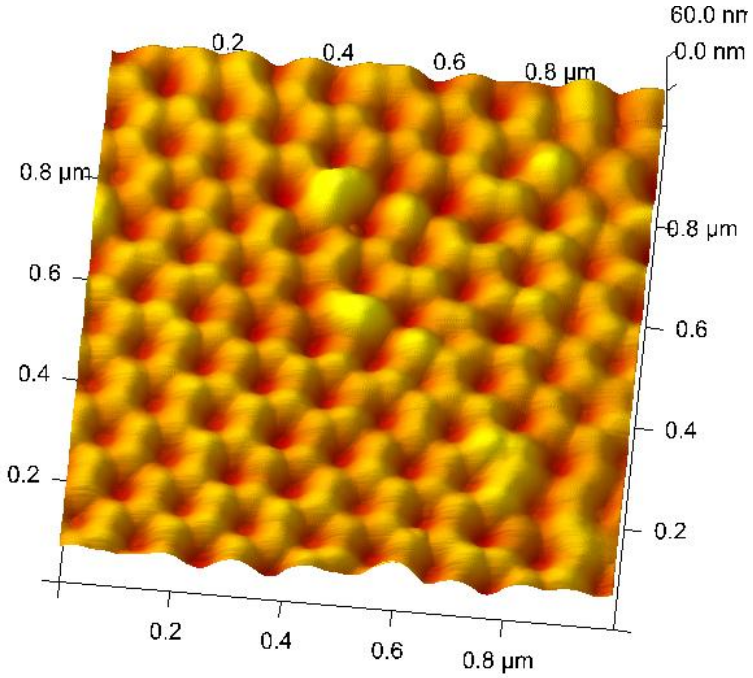

Figure 4.1a, b and c Top view AFM images of the aluminum surface taken after dissolving out the anodic alumina film in hot chromic/phosphoric acid. Diameters are ~10nm, ~20nm and ~50nm respectively.

Next, the organic molecules are dissolved in a liquid solvent and electrospray ionization is used to deposit them *selectively* within the pores. In the electrospray process, charged droplets are generated at the tip of a metal needle (or pipette with a wire immersed in the liquid) and are subsequently delivered to a grounded target (e.g. the alumina film). The droplets are derived by charging a liquid typically to 5-20 kV vs. the target, which leads to charge injection into the liquid from the electrode. The charged liquid is attracted to the ground electrode of opposite polarity, forming a so-called Taylor cone at the needle tip. Droplets are formed when electrostatic forces between the charged liquid and the ground exceed the liquid's surface tension. If the liquid is relatively volatile, the solvent liquid will evaporate and a dry stream of solute ions will be deposited

onto the target. In the case of the nanoporous alumina target, the insulating alumina regions will quickly charge up until the charge density on the alumina surface produces an electric field equal and opposite to the externally applied electric field. The surface charge on the alumina template will force the electric field lines to penetrate into the pores and terminate on the back metal contact. As a result, the electrosprayed species is *selectively* deposited only within the pores and not outside it

4.3. Results and Discussion

The fluorescence spectra of the samples are then obtained at room temperature. We made the following observations:

⇒ There is a giant red- or blue-shift in the fluorescence peak of molecules confined within the pores. Both the magnitude and the sign of the shift is molecule-specific, i.e. different molecules experience different relative shifts $\Delta\lambda / \lambda$ (λ is the wavelength at which the fluorescence of the unconfined molecule peaks). This molecular specificity allows us to discriminate between different molecules and provides the means for molecular recognition.

⇒ The fluorescence efficiency of the confined molecules increases many fold. The increase is monotonic with decreasing pore diameter.

The latter feature is caused by two effects working in concert. The first is "metal-enhanced-fluorescence" (MEF) where interactions of fluorophores with the nanotextured metallic surfaces (which, in our case, are the aluminum pits at the bottom of the pores) increases the radiative recombination rate and therefore the quantum yield of photons,

resulting in an increase in the fluorescence efficiency. The quantum yield increases due to local electromagnetic fields caused by plasmon resonance associated with the metallic surfaces. The second effect is "waveguiding" by the pores, which directs the plasmonic electromagnetic fields along the length of the pores and couples them into the molecules very effectively, resulting in a very large increase in the quantum yield of photons. Thus, both the metallic pits at the bottom of the pores and the pore walls play an active role in increasing the luminescence efficiency. The electromagnetic fields inside the pores are actually evanescent since the pore diameter (10-50 nm) is certainly smaller than the wavelength of the electromagnetic modes. However, because the pore lengths are only about 1 μm, the evanescent modes can still traverse the entire length of the pores and couple to all the molecules.

Since the electromagnetic waves are guided along the pores, the pores with the smallest diameter will have the highest concentration of electric field. Therefore, we expect to observe the highest increase in the quantum yield of photons in the narrowest pores. This expectation is borne out by the experimental observations. Indeed the increase in the luminescence intensity is maximum in the 10-nm diameter pores and minimum in the 50-nm diameter pores. Reference [50-52] pointed out that the electromagnetic field caused by the metallic surface can induce a red- or blue-shift in the fluorescence peak because of the Stark effect which renormalizes the energy levels within a molecule in the presence of an electric field. This renormalization occurs since the electric field alters the dipole moment of the molecule [53]. That changes the energy gap between the HOMO and LUMO levels, causing a blue- or red-shift in the fluorescence

peak depending on whether the energy gap expands or shrinks. Obviously the sign (red or blue) and the magnitude of the shift will be molecule-specific since the energy gap will increase in some molecules and decrease in others (depending on their dipole moments). That is exactly what we see. This molecular-specificity can be exploited for bio- and chemical sensing.

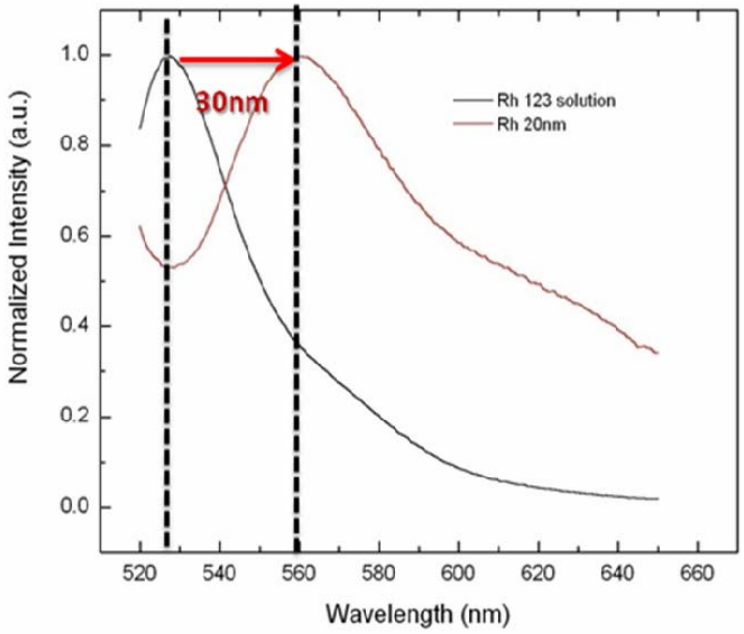

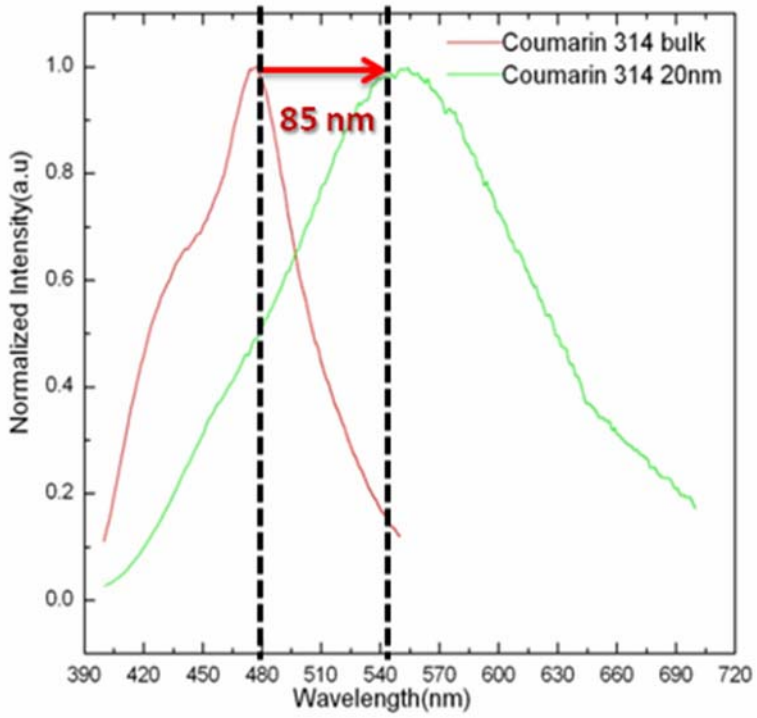

Figure 4.2 Emission spectra of organic fluorophores in pores showing giant red shifts. Emission spectrum of (a) Rhodamine 123 and (b) Coumarin 314 in pores of diameter 20 nm compared to the emission spectrum of the corresponding bulk specimens.

In Fig. 4.2, we show the red shift in the fluorescence spectra of Rhodamine and Coumarin molecules that are observed when the molecules are electrosprayed within 20-nm pores. The relative red-shift $\Delta\lambda / \lambda$ (λ is the peak fluorescence wavelength of a bulk sample) is much larger in Coumarin (16%) than in Rhodamine (5.5%). If Stark shift is the cause, then we naturally expect Coumarin to have a larger relative shift than Rhodamine since the former molecule has a much larger dipole moment.

In Fig. 4.3, we show the fluorescence spectra of Rhodamine 123 (confined in pores) as a function of pore diameter. In this measurement, the excitation intensity was kept constant and the amount (or volume) of deposited material, determined by the duration of

electrospraying, was also kept constant. Therefore, the measured intensity of fluorescence is proportional to the luminescence efficiency, which clearly increases with decreasing pore diameter. This happens because the plasmonic electromagnetic fields are more concentrated within the narrower pores.

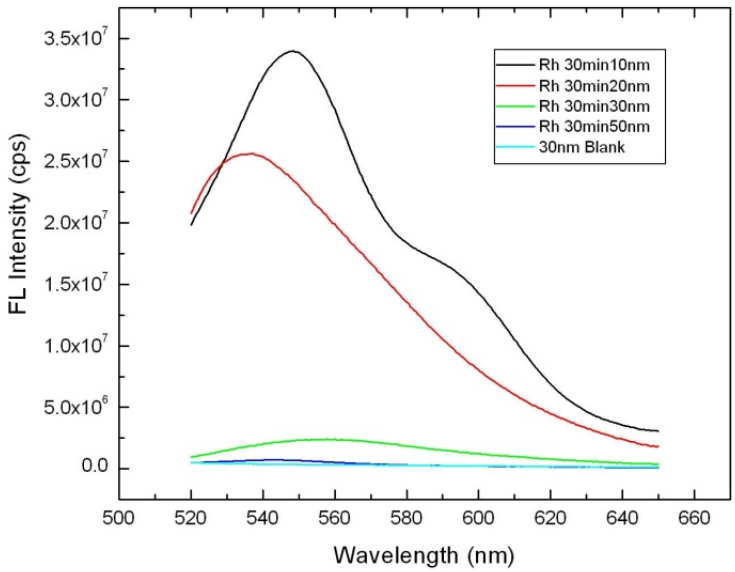

Figure 4.3 Luminescence efficiency and Stark shift as a function of pore diameter. (a) Dependence of the emission intensity (for fixed excitation intensity) and Stark shift of Rhodamine 123 on the pore diameter.

In Fig. 4.3, we also see that the red shift increases with decreasing pore diameter. This is consistent with the observation that the smaller pores have the larger electric field. The larger field naturally induces a larger Stark shift, which explains why the red shift increases with decreasing pore diameter. It may appear that the 30-nm diameter pores are an exception to this trend, but the fluorescence peak of the 30-nm sample is so broad that

we cannot precisely locate its peak. All other samples follow the trend that smaller diameter pores cause a larger Stark shift.

In Fig. 4.4, we show the normalized emission spectra of dipicolinic acid (DPA) molecules electrodeposited in 20 and 50 nm pores. The 50-nm samples show no significant shift in the peak frequency, but the 20 nm samples, show a significant *blue-shift* of 50 nm. Obviously, the concentration of the plasmonic electromagnetic field in the 50 nm pores is not enough to cause a significant blue shift, but it is enough in the 20 nm pores. DPA is an important constituent in bacillus spores (e.g. anthrax) and the ability to engineer its emission spectrum by spraying it into narrow pores provides an important tool for detection and identification of DPA.

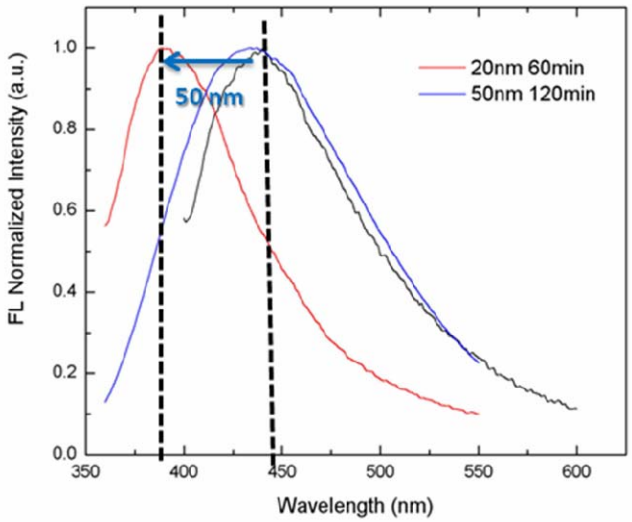

Figure 4.4 Emission spectra of dipicolinic acid (DPA) as a function of wire diameter.

The molecule specific red- and blue-shifts can also be used to resolve different constituents in a mixture, even if they have overlapping emission spectra (and are therefore optically indistinguishable) in a neutral environment. In Fig. 4.5(a) and 4.5(b), we show the emission spectra of bulk tryptophan and tyrosin along with the spectra obtained when the molecules are electropsprayed within 50-nm diameter pores. The spectra of bulk molecules overlap in the frequency domain, making trypotophan and tyrosin optically indistinguishable. However, when a mixture of these two biomolecules (in equal molar parts) are electrosprayed within 50 nm pores of an alumina film, we induce a 40 nm red-shift in the peak wavelength of tryptophan and 120 nm red-shift in the peak wavelength of tyrosin. As a result, we see a double peak structure in 50 nm pores (Fig. 4.5(c)) where the high energy peak is easily identifiable with tryptophan and the low energy peak with tyrosin. In bulk form, the mixture does not exhibit a double peak structure as seen in Fig. 4.5(c), but when it is electrosprayed into 50 nm pores, the double peak structure immediately shows up. Thus, we have demonstrated a powerful technique that allows us to resolve these otherwise indistinguishable compounds using fluorescence spectra. This can lead to a new technology for bio- and chemical-sensing.

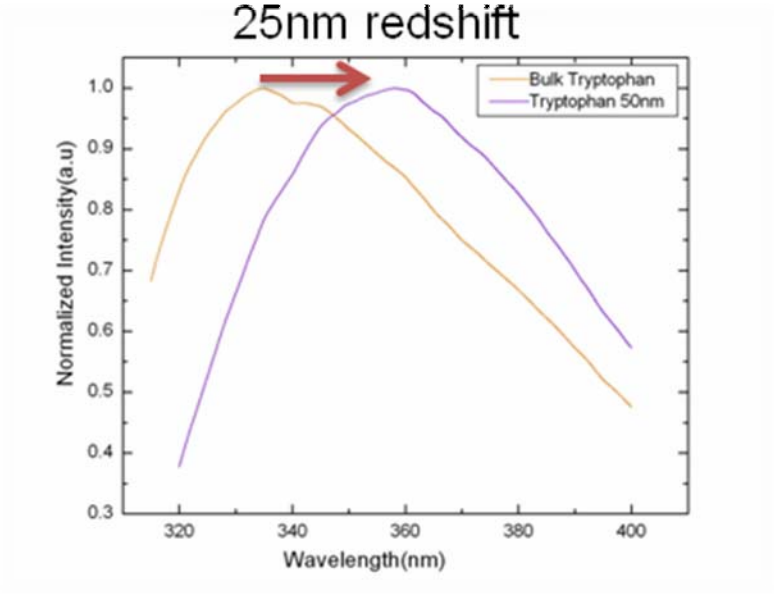
25nm redshift
Bulk Tryptophan
Tryptophan 50nm
Normalized Intensity(a.u)
Wavelength(nm)
1.0
0.9
0.8
0.7
0.6
0.5
0.4
0.3
320
340
360
380
400

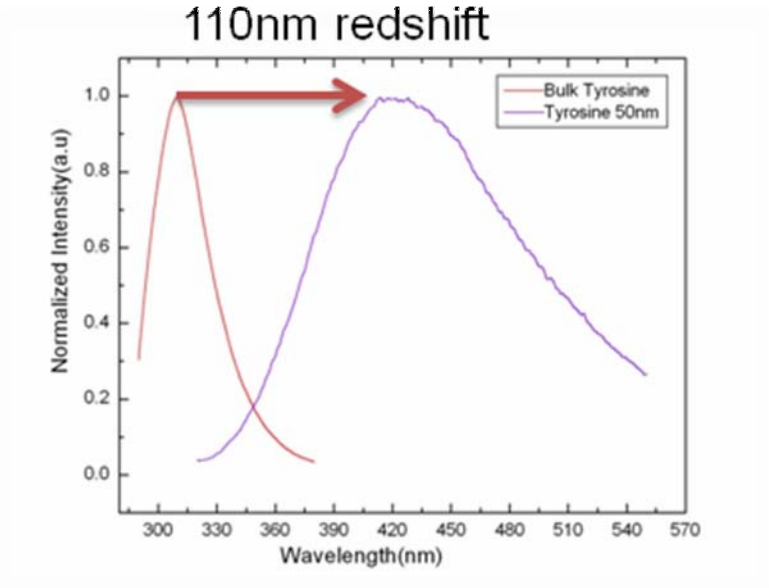
110nm redshift
Bulk Tyrosine
Tyrosine 50nm
Normalized Intensity(a.u)
Wavelength(nm)
1.0
0.8
0.6
0.4
0.2
0.0
300
330
360
390
420
450
480
510
540
570

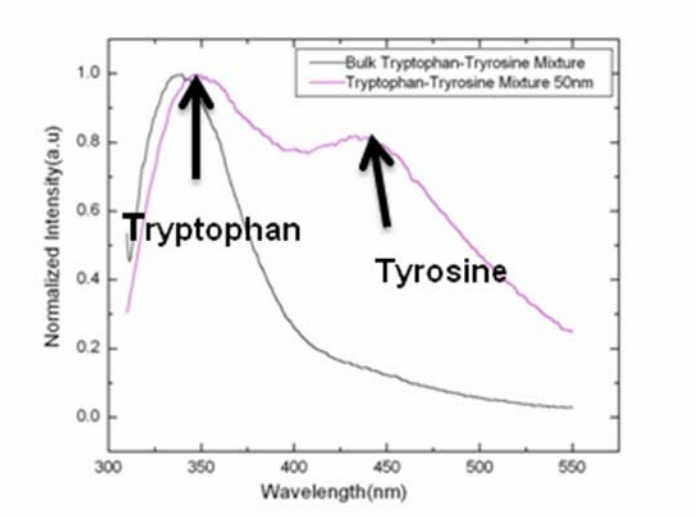

Figure 4.5 (a) The emission spectra of tryptophan in bulk and in 50 nm pores, (b) the emission spectra of tyrosin in bulk and in 50 nm pores, (c) the emission spectra of equal molar parts of tryptophan and tyrosin showing a single peak structure in bulk but a double peak structure in 50 nm pores

4.4 Conclusion

In conclusion, we have demonstrated that confining organic fluorophore molecules within anodic alumina pores that have exposed nanostructured aluminum at the bottom increases the fluorescence intensity and induces molecule specific giant frequency shifts in the fluorescence peak. While the former increases the detectivity, the latter increases the selectivity of molecule sensors based on fluorescence. The molecule specific frequency shifts in the fluorescence spectrum also allows us to deconvolve the spectra of two different constituents in a mixture that have overlapping spectra. This can be used for molecular recognition, and ultimately bio- or chemical detection.

CHAPTER 5. Self assembly of stepped hollow oxide nanostructures with plasmonic -photonic properties

5.1 Introduction

Self-assembly of nanostructure has recently drawn a lot of attention due to their wide range of application. Especially, recent development in the field of fabrication has spurred development in wide range of fields ranging from photonics to fuel cells. While 1d/2d metal nanostructure has drawn a lot of attention [54-58] and easy to fabricate, self-assembly of oxide nanoparticle or composite metal-oxide remains challenging [59-61]. Recently, O. Toader et.al.[62] showed how 3d photonic effect can be obtained by having structure in slated pore nanostructure. Using photolithography and plasma etching they showed how these structures could be fabricated. Even though this process is well established the process remains expensive and time consuming. Therefore, self-assembly process, where we can easily manipulate fundamental infractions of materials remains the simplest.

While wide variety interaction among the different phases of materials exists, oxidation and its effect on stress always has been a subject of intense research among the scientific communities. For example, Aumann et. al.[63] found that increase surface area lowers the oxidation activation energy. Also, Zhou et.al.[64] recently showed how terraced hollow oxide can be formed due to high temperature oxidation of

Cu. Recently, chemical oxidation, especially electrochemical oxidation of aluminum has drawn a lot of attention due to its potential to create useful nanostructures [65-67]. In this process, using appropriate current and voltage very ordered porous structure is created by electrochemical oxidation. In all of the previous studies, films or foils with wide range of thicknesses were studied with the goal of obtaining and understanding ordered porous structures.

Here we study nanostructure formation due to the oxidation of nanodots. Since wide range of nanodots can be formed using appropriate substrate and metals a very wide opportunity remains to form wide range of 2d/3d structure, we show a shape transition in its structure during oxidation by forming cavity with "staircase" type interior. We choose aluminum as fundamental elastic data about aluminum and its oxide is readily available. Oxidation of well-separated nanodots is interesting because complex stress conditions can form different size and shape on different substrates [68].

5.2 Experimental Details

The structure is mainly fabricated in two steps; self-assembly of aluminum nanodots from thin film by rapid thermal annealing and anodization of nanodots to form staircase-like structure. About 10 nm of gold was thermally deposited on glass wafers followed by 50, 70 and 100 nm of aluminum thin film. The samples were then annealed in a fast thermal anneal chamber to form the nanodots. The purpose of the gold layer is simple: to provide conduction paths between the power supply and the nanodots. Any conducting material can be used as long as the melting point of the material is higher than

the melting point of nanodot forming material. This is simply to avoid any interdiffusion and open circuits during anodization. We found that 50 nm is the lowest thickness where the nanodots are organized and big enough to form semi-organized structure. Detail of the deposition conditions can be found in [69]. The samples were annealed at 600 ◦C hence very fast diffusion within aluminum is attainable while gold is reasonably stable. It is possible to have some interdiffusion take place while the dots are forming but the process does not effect the formation of nanodots. The process results in formation of aluminum nanodots as shown in figure 5.1. Then the sample was anodized in 3% oxalic acid for 5min

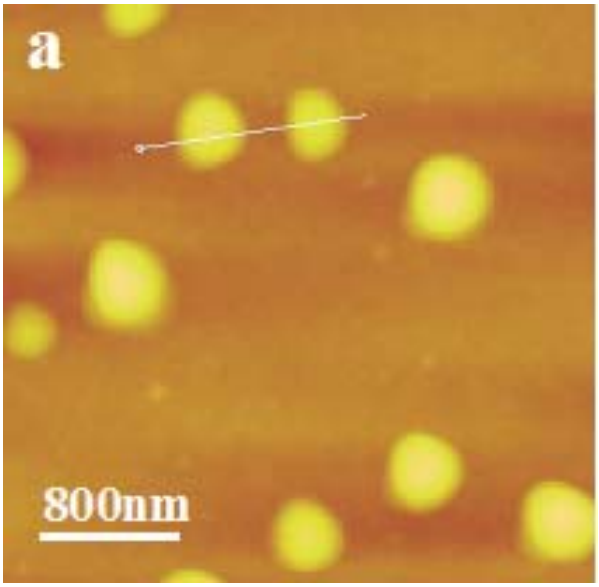

Figure 5.1 AFM image of Al dots on gold film

This process resulted in formation of alumina nanostructure with staircase-like interior. We have verified that dot formation and alumina nanocrystal formation can be controlled up to 100 nm aluminum thickness. Optical properties were verified with a UV–visible

spectrometer and Fourier transform infrared spectrometer (FTIR). To identify typical surface processes for these structures, we calculate the height–height correlation function (HCF). The advantage of this method is that without knowing detail of the interaction we can have better understanding of interface growth processes based on internal symmetries and dimension.

5.3 Results and Discussion

Figure 5.2 shows formation of alumina with stepped interior. The dots were about 60 nm in height; therefore, the height of the oxide structure is expected to imitate the nanodot height.

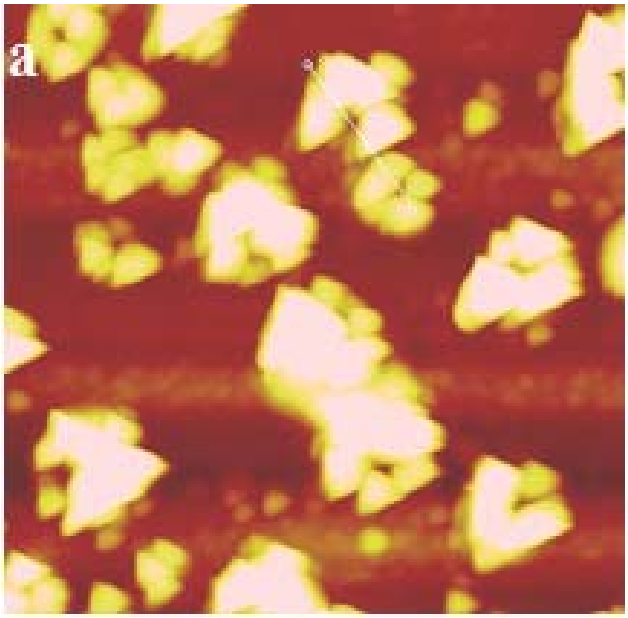

Figure 5.2 AFM image of alumina with stepped interior

Later, we will show that the steps are nonmonotonic and faceted, hence showing characteristics of a 'devil's staircase' [70]. Since nanodots are self-assembled by annealing the thin films and by manipulating the fact that aluminum has very low melting point, some interdiffusion is possible and dot size can vary resulting in an erratic pore structure. However, for 100 nm thick aluminum film, nanodots are well formed and separated and when anodized, the pores are well formed and dense. Figure 5.3 shows an alumina structure formed with well-structured interior from bigger nanodots (100 nm).

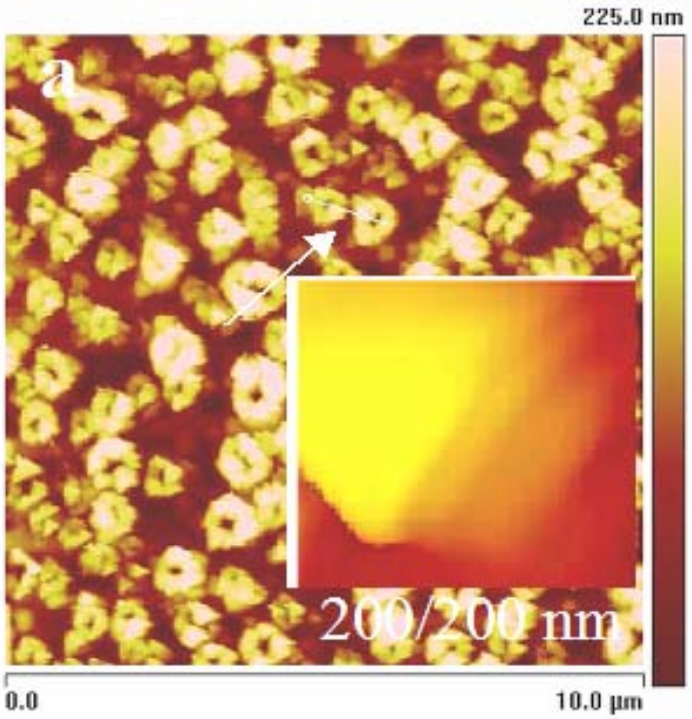

Figure 5.3 AFM image of alumina structure for 100nm Al dots

The formation of these structures is very similar to that of other oxide systems. For example, when copper films are oxidized, instead of forming uniform layers they tend to

grow as oxide islands and they can be self-limiting after certain thicknesses [71]. For our case, we can assume similar situations, where the primary reason for formation of the structures is stress inside the oxide. For compressive stress it is required that the volume of metal ions in the oxide is bigger than the volume of metal in the metal. For most metal this is true and for aluminum the value is 1.28. Therefore, for this case the stress is compressive. Generally for thin film systems, oxide forms through random nucleation sites. For electrochemical oxidation the sites are preferential. For example, tips of the nanodots have higher electric field and will oxidize faster than the sidewalls. Therefore, stress will build up faster at the top than on the sidewalls. Since the nanodots have triangular/conic profiles less force will be required to cause plastic slip at the top. Hence, due to fast build up of high stress, the nanodot tips will have bigger openings than the bottom and thus should have tilted pore walls. The observed step height is also consistent with previous observations made for planar film [72].Figure 5.4 shows the roughness exponent calculation based height–height correlation function. Figure 5.4(a) shows two exponents for nanodots, formed with 50 nm thick aluminum thin film and figure5.4(b) shows exponent values after anodization including the thicker (100 nm) case. As seen in figure 5.4(a), the global roughness exponent is >1.5. The value of $\alpha > 1$ generally suggests that the surface is super-rough [73]. In this case the local surface width does not saturate and crosses over to a different behavior. Surface processes exhibiting such behavior are generally called anomalously scaling [74]. Although there is no well understood theory of anomalous scaling, it has been suggested that it must be due to non-local effects [75].

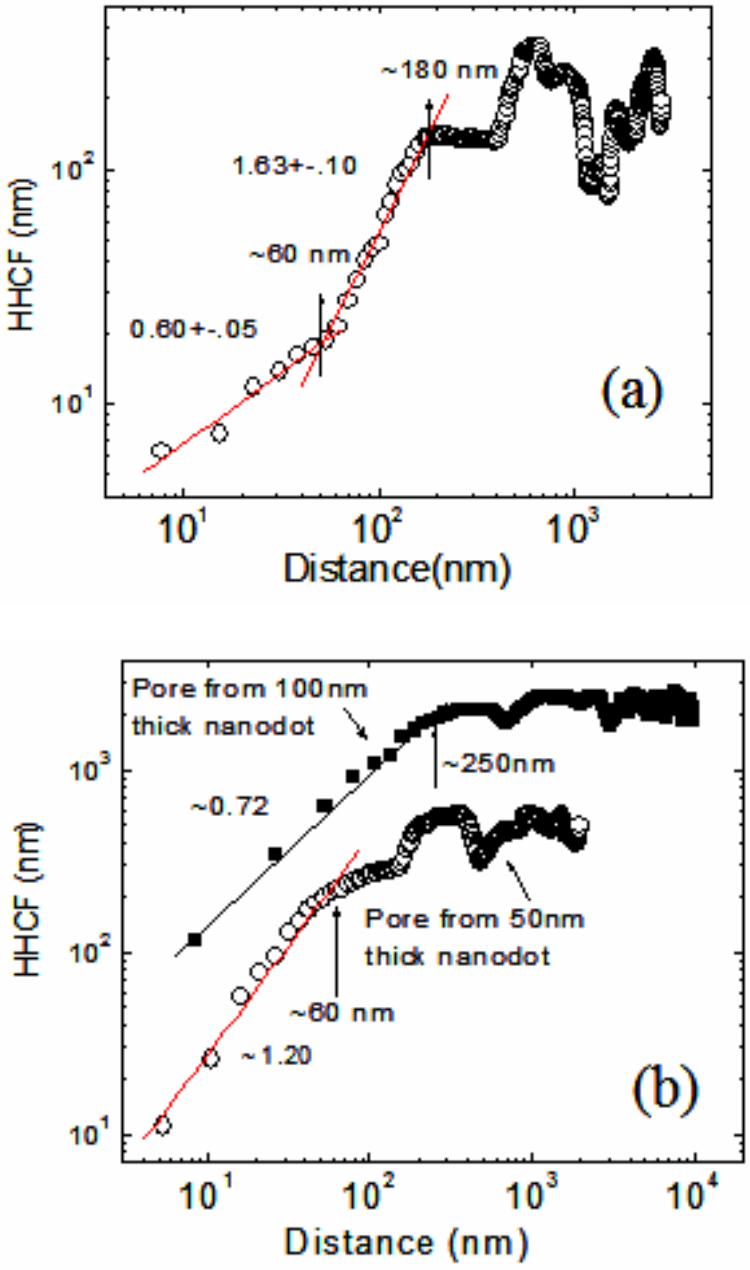

Figure 5.4 (a-b) HHCF vs Distance calculated using height–height correlation function.

Aluminum nanodots formed by annealing close to the melting point have several such effects. An important one is rapid jumping in the interface position. Observe that

nanodots are well separated, with 60 nm height consistent with this case. Therefore, with more dense and rough structure the anomalous scaling should vanish. We find that this is indeed the case. After anodization we find that the system lacks anomalous scaling and the roughness exponent drops even further for denser anodized nanodots as seen in figure 5.4(b). The detail of surface processes for nonlinear and linear cases described by Das Sarma *et al* [76] using Monte Carlo simulations in 2D follows. For the linear case, it is found that only isolated atoms can diffuse and will stick to the nearest kink site. Therefore, movement of clusters should be minimal during oxidation and as they touch other oxidized sites they become pinned and aggregate until the compressive stress is high enough to cause slip. For small nanodots (50 nm), this is not immediately visible due to large and sudden interface fluctuation. For more dense and ordered structure at 100 nm structure level, this is clearly seen.. The fractal dimension agrees well with the cluster– cluster aggregation model [77]. We should mention here that the model only provides a general description of the process, not addressing the intricate detail. In particular, formations with tilts, different facets and disorder evolving are not taken into account. Figures 5.5(a) and (b) show some representative step profiles for various size dots. Clearly seen steps are not correlated and have various facet angles. Fast Fourier transformation (figure 5.5(b), inset) of the profile figure 5.5(b) shows that the steps are non-monotonic; therefore they are 'devil's staircase' type. Figure 5.5(c) clearly shows steps with well-defined cavities.

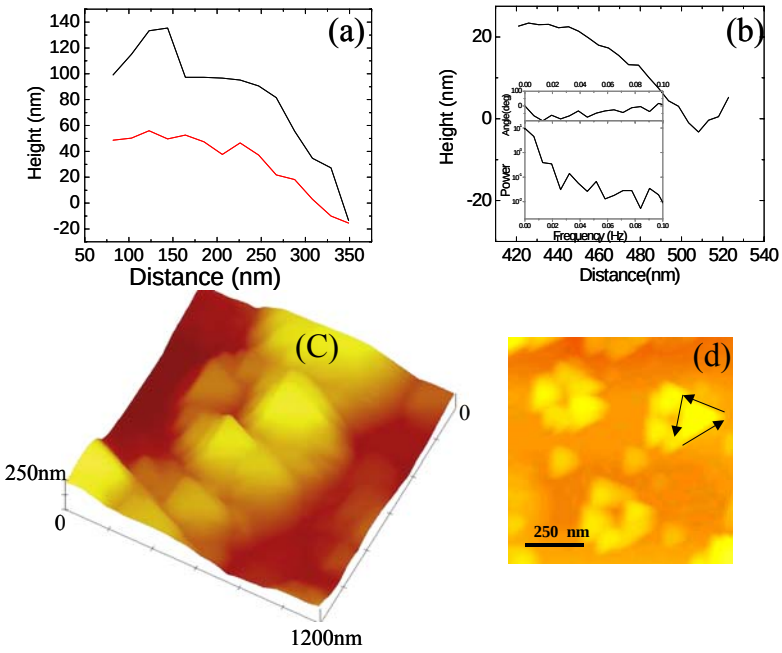

Figure 5.5 (a-d) Step profile and AFM image of interior step structure.

This observation is different to previous observations of structures found for high temperature oxidation. Formation of a 'devil's staircase' also suggests that a competing mechanism is present in the system that led to the formation of these structures. Figure 5.6 shows reflectivity measurements at various steps of the alumina formation process. We find a drop in reflectivity by 90% in UV–visible range. We find that the reduction is over a broad range of the spectrum, with absorption.

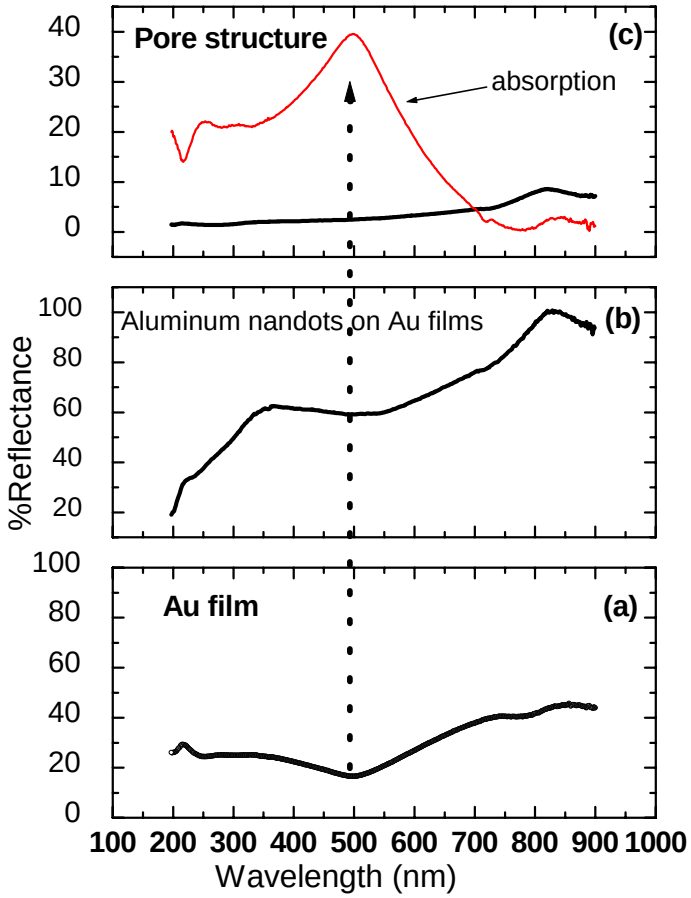

Figure 5.6 UV reflectivity measurements for step profile structure

We believe one of the main reasons is the location of Au thin film beneath the pore structure. Figure 5.6 shows that Au itself can reduce reflectivity over broad range of wavelengths, by absorption of 40%. This is consistent with the fact that oxide nanostructure covers about 70% of the surface. Coupling between these structures can result in an observed broadening. While our resources limit us, other conducting material or conducting oxide can eliminate this problem.

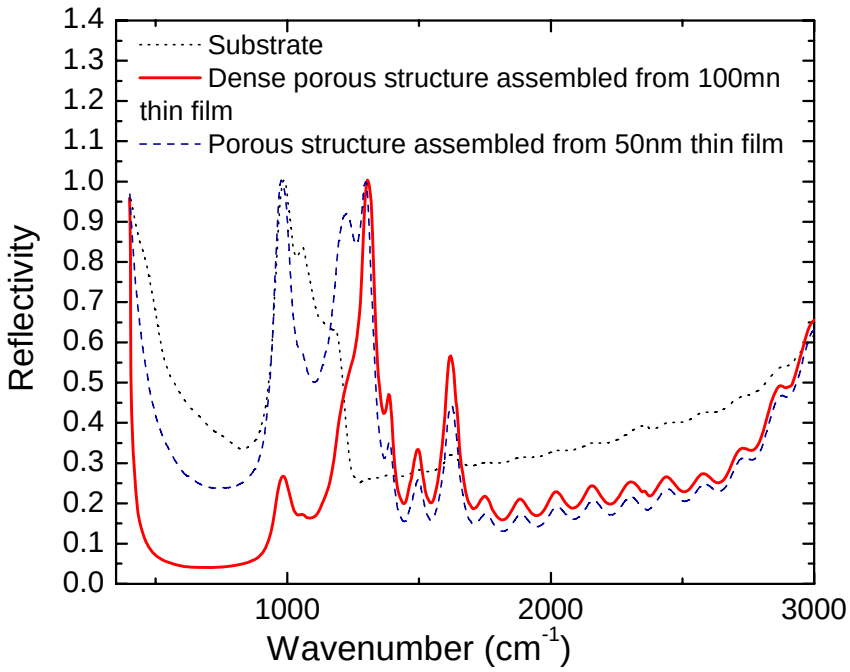

Figure 5.7 FTIR spectrums for plain glass and step profile structure on glass

Figure 5.7 shows the FTIR spectrum of the structure. The FTIR spectrum for glass substrate is also shown for comparison. We believe that the high reflectance in the IR is cavity resonant type. The first signature is the asymmetric nature of the transmission, indicating cavity resonance and Fabry–Perot oscillation coupled. The second indication came from experimental reflectivity as shown for less dense cases (50 nm film). Clearly seen are the cavities being more dispersed as the reflectivity is more coupled to the background, which in this case is glass.

5.4 Conclusions

In conclusion, we show the formation of large nanodots by driving the interface close to its melting point. Using this for nanodots we have shown a simple method for selfassembling dielectric nanocrystal with slanted pore 'staircase'- like interior. The reflectivity results suggest that complexcoupling phenomena exist, between the cavities, and these structures can act as a photonic material. In the light of recent development in complex photonic structures [78].We believe very complex dielectric structures can be made using metal that forms different crystalline facets. We have left out two effects in this work. One is Au/Al interaction in terms of nanodot formation and island–island interaction for size distribution. Since the heat of melting [79] for Au (17.8 kJ mol−1) is 1.5 times that for Al for a short anneal, we do not expect enough interaction to affect the nanodot formation. While the effect of surface energy and substrate–film stress interaction on the density of nanodots can be similar to that for other low temperature annealed nanodot systems, melting point driven bimetallic systems require more rigorous schemes.

CHAPTER 6. Fluorescence spectroscopy and surface analysis of nanoscale organic light emissive thin films

6.1 Introduction

Organic materials continue to attract scientific and technological interest due to its easy applicability to fabricate light emitting diodes and large area flexible display with wide range of advantages like fast response time, low power consumption and structural simplicity [80-83]. With continued improvement in material and process the improvements are showing feasibility for panel lighting. However, a wide range of fundamental issues needs to be addressed in order to optimize any device structure. From a materials point of view, formation and transport of spin and singlet and triplet excited states and effect of surface/interface morphology remains a strong focus [84-86].

Organic light-emitting diode (OLED) based on aluminum tris(8-hydroxyquinolinate) (Alq3) ,gained huge interest due to its properties such as relative stability, easy synthesis, good electron transport, and emitting properties [87-90]. Recently, systematic investigations of the structural and optical properties of Alq_3 in the solid state, as well as of the influence of the preparation conditions an deposition rate on these properties were carried out [91]. Curioni et al. [92] showed using ab initio calculations, the coexistence in the thin film of two geometrical isomers, meridianal (mer-Alq_3) and facial (fac-Alq_3). According to the above results, the facial isomer is less

stable in energy than the meridianal [93]. Along with the well-known three crystalline phases of Alq3 (α,β,γ), the existence of δ phase showing blue shifted luminescence was reported [94]. While most of the studies are available on true device structure, few studies are available on surface properties of this material with thickness dependence [95], especially with high-resolution surface microscopy. Therefore, understanding surface evolution and its correlation to optical properties requires further studies.

In this work we report surface evolution and optical properties of Alq3 deposited by energetic cluster mask [96]. By calculating fractal dimension [97-100] using scaling properties we identified typical diffusion mode of the surface. We also report blue shift for low thickness percolation type cluster.

6.2 Experimental Details.

Alq_3 with varying thicknesses has been thermally evaporated on ITO substrates. ITO about 1200A thick coated onto glass substrates about 1.1 mm thick and 2" x 3" in area have been purchased from Delta Technologies Ltd. The resistance of the substrates is about 30-60Ohms. The substrates are then cut into smaller dimensions about 1" x ½" with the help of a diamond scribe. The substrates are scribed on the glass side to minimize contamination of the ITO surface from the glass particles. The cut substrates are then cleaned by ultrasonic agitation in a detergent solution and thoroughly rinsed in DI water. The substrates are then heated on a hot plate to about 80°C for 30minutes to remove the moisture on the surface. The substrates are then loaded into the vacuum chamber. The evaporation of Alq_3 is carried out in high vacuum ~2 $x10^{-6}$ Torr by heating

the source to a temperature above the melting point. The deposition rate is maintained between 0.2- 1A/sec by accurately controlling the current passing through the evaporation source with the help of SQC122 deposition controller from Sigma Instruments, Colorado. An energy cluster mask has been used to obtain smooth films on the substrate . The surface was characterized with atomic force microscopy [101] in a phase imaging mode (DI) and normal mode. In phase imaging, a variant of tapping mode AFM imaging, the phase lag of the cantilever oscillation relative to the signal sent to the cantilever's piezo driver is used as a basis for image generation. Phase images can be generated as a consequence of variations in material properties such as adhesion or friction thus shows superior contrast and a qualitative compositional variation of the surface. Photoluminescence data was taken in a matrix form using Xenon lamp as an excitation source with auto correction for reflection. Infrared transmission measurements were taken at room temperature using Bruker equipment. The thickness of 5,10,20 and 100nm were chosen to obtain surface properties over 2 decades, which is widely studied in a true OLED device format.

6.3 Results and Discussion.

Figure 6.1 shows atomic force microscopy image of 5, 10, 20 and 100nm thick films in phase mode. At 5nm the films are uniform with no grain formation but percolation boundaries with small pinholes/nanovoids are seen. Influences of nanovoids on photoluminescence properties were previously reported but clear picture of density/size was not reported. At this thickness the nanovoids are uniformly distributed

throughout the film. As the grain boundaries are formed the nanovoids are prominent only at the triple junction of the grain boundaries . For all thicknesses the phase contrast is 20° indicating unchanged film physical properties over all thickness, compared to 90° with wide variation seen in other system.

Figure 6.2a and figure 6.2b shows the 3d images of 5nm and 100nm film. Consistent with phase imaging data from figure 1, at low thicknesses there are several distributions of grain sizes are seen. At higher thickness a single size distribution is prominent. This is also seen in height-height correlation function (HHCF) show in figure 6.2c and figure 6.2d.

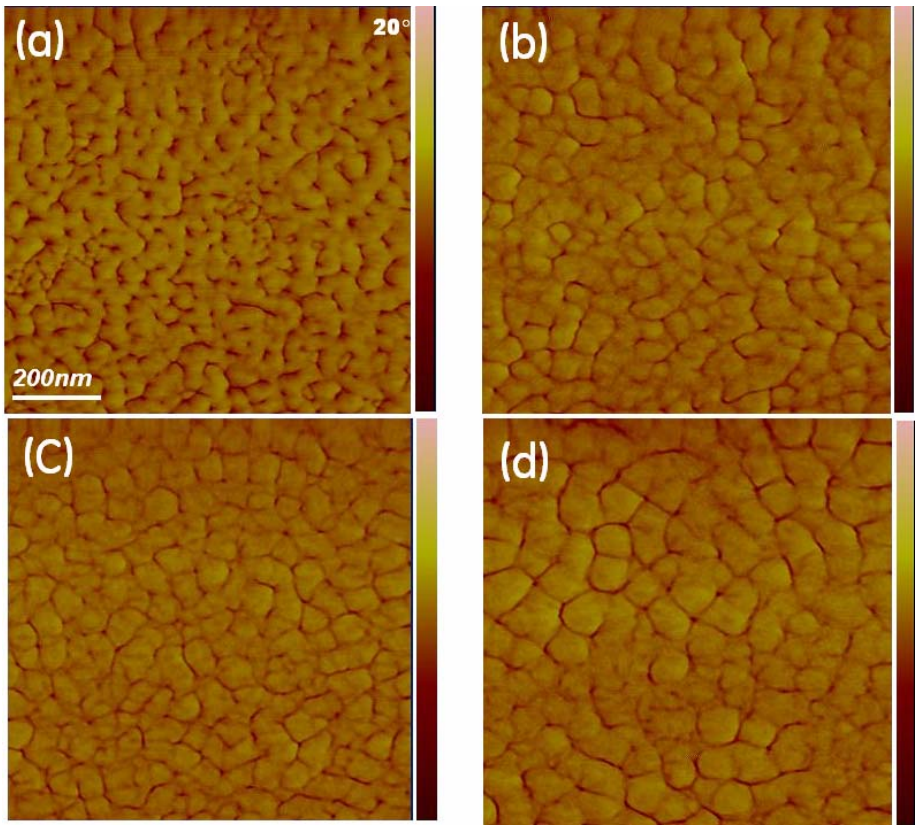

Figure 6.1 AFM (phase) image of 5, 10, 20 and 100nm Alq3 on ITO

For any arbitrary surface the HHCF scales as HCF~ r^{α}. And fractal dimension is given by D= d- α. Figure 6.2c shows fractal dimension of the surfaces for all thicknesses except for 5 nm. Figure 6.2d shows fractal dimension of the film at 5nm. The bump at the lower window length consistent with the image in figure 6.2a, where wide distributions of grains are seen.

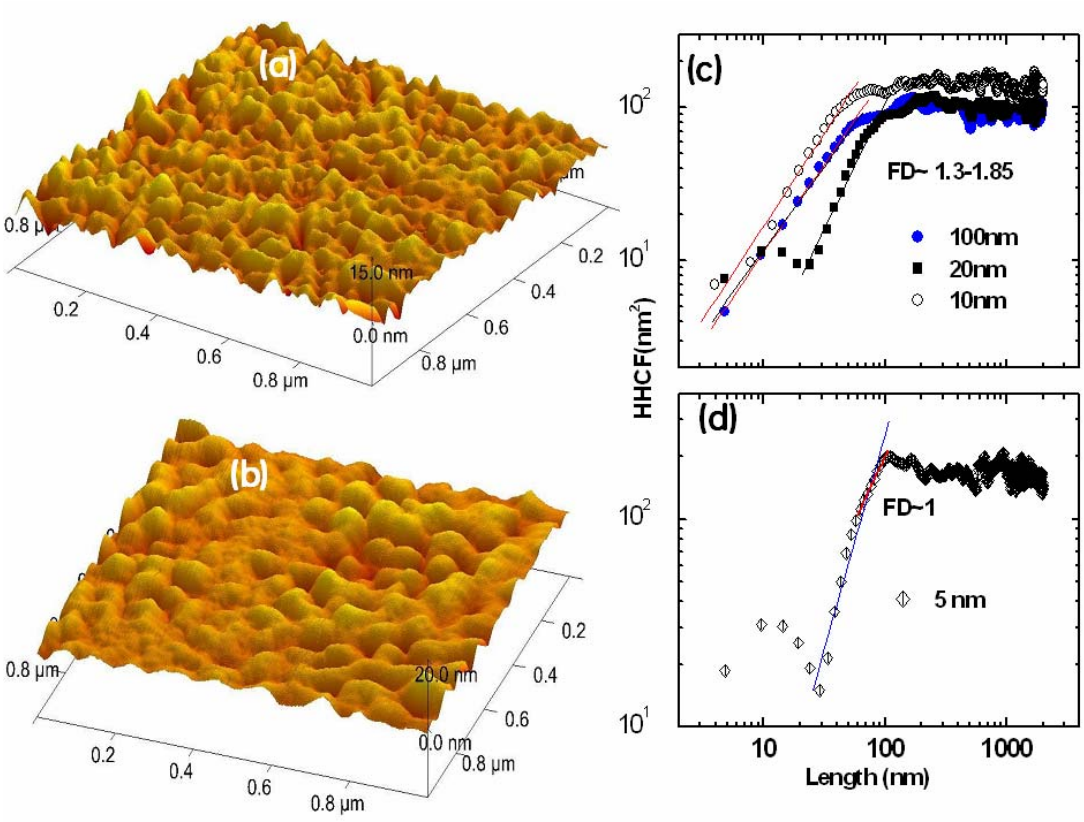

Figure 6.2 (a-d) 3D AFM image and HHCF plots of 5nm and 100nm Alq_3 on ITO

For thicknesses > 10nm the fractal dimensions have wide distribution but consistent with diffusion limited aggregation process. At 5nm the fractal dimension can imply a different growth mode where thickness dependent transition is observed. The correlation to FD to

photoluminescence shift shows that shift is very likely to be surface state and growth mode related and increases in max peak intensity is intrinsic related to interface and orientation/phase as discussed in last paragraph.

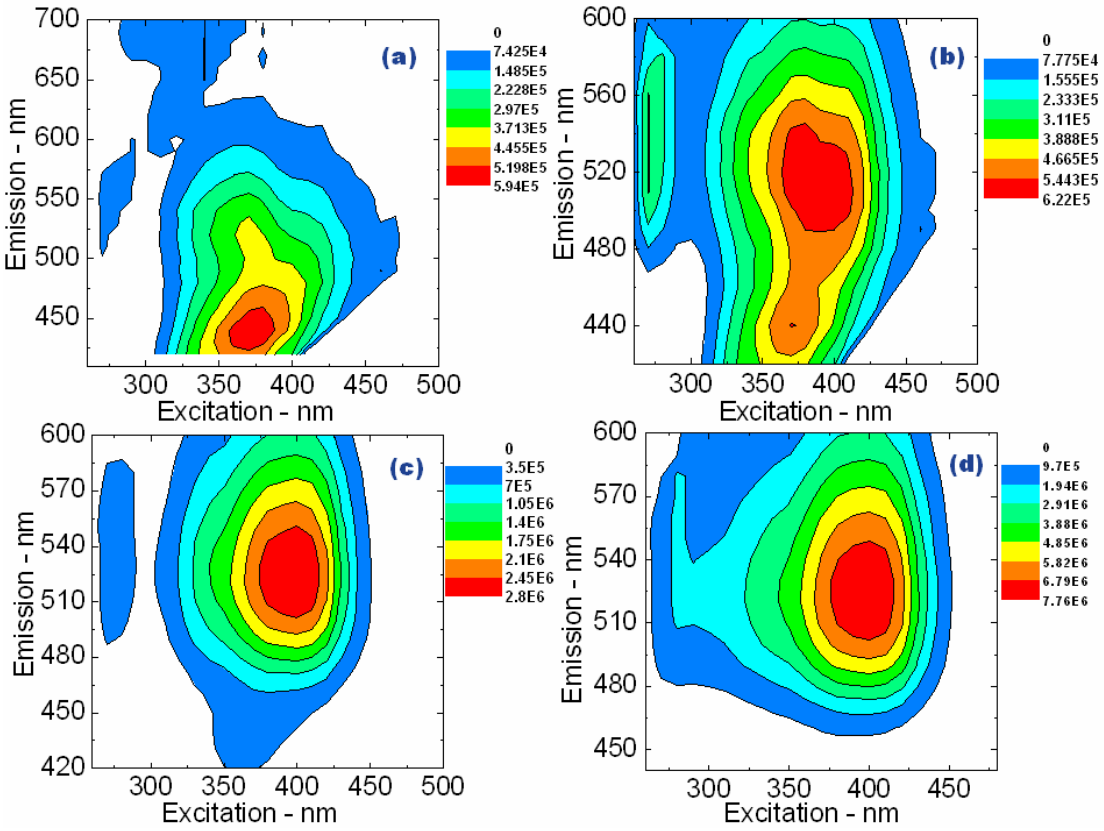

Figure 6.3 (a-d) Matrix plots of PL spectra of 5, 10, 20 and 100nm Alq_3 on ITO

The classification in terms of fractal growth mode has excellent correlation to photoluminescence data. In figure 6.3a shows photoluminescence data in matrix form for 5nm thick film. It is interesting that the peak luminescence is shifted to the lower wavelength compared to the other thicknesses as seen in figure 6.3b (10nm), figure 6.3c(20nm) and figure 6.3d(100nm). The shift calculated to be 0.4eV. In one of the previous study Gordon et.al showed that at the monolayer level (~1nm) thin film of Alq_3 can blue

shift due to reduced intermolecular interaction at the ultra-thin range. They also showed the films exhibit bulk like luminescence value >2nm. Their model based approximate dielectric medium consistently predicted the observation.

To further verify any consistent trend based on thickness, we performed infrared transmission measurement of the all thickness as seen in figure 6.4.

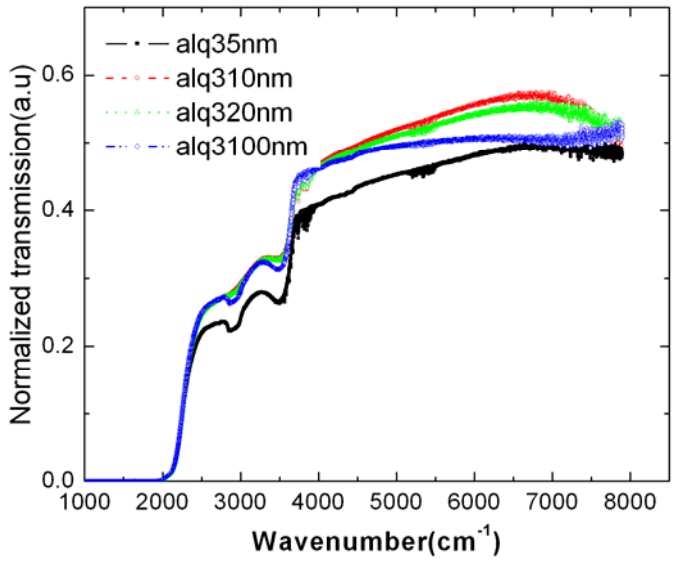

Figure 6.4 FTIR spectra of 5, 10 20 and 100nm Alq3 on ITO

Infrared transmission measurements can give us useful information on absorption features and optical conductivity of the polymer films [102]. Optical conductivity is related to band gap and transport properties; therefore the data suggests the films have very similar carrier concentration [103]. Interestingly, 5nm is less transmisive than the other thickness. The vibrational feature at 3000cm^{-1} is not consistent in terms of thickness since it reappears for 100nm. It is possible to have similar effect at 5nm due to distribution of grain formation, as seen in the image and HHCF of figure 6.3a and figure

6.3d. In one of the previous studies Barun et.al. shown that δ-Alq3 formation at the surface at high temperature can exhibit blue shift of ~0.2eV, which is lower than what we have observed. Recently, Levichkova et.al.[104] showed that for isolated molecules in solid state matrix, blue shift of up to 0.3eV can be observed. All these studies give us some idea of the complicated interaction in the system, which is also seen yet in other effects as summarized in figure 5.

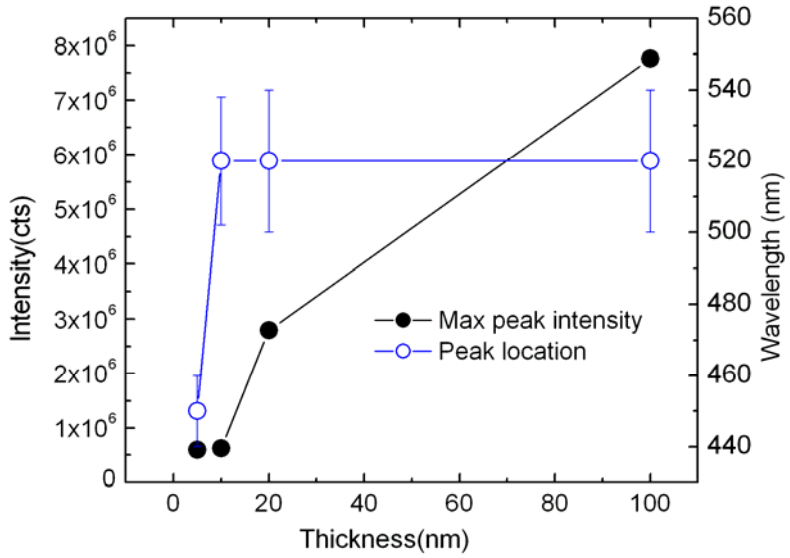

Figure 6.5 Intensity Vs Thickness of Alq_3 on ITO

Figure 6.5 shows increase in peck intensity with thickness after 10nm and shift in peak location after 5nm. The shift in peak location corresponds to fractal dimension calculation. Therefore it is likely that some surface effect is mainly responsible for peak shift. The increase in intensity with thickness is observed and reported before for other organic molecular system . The trend in the peak intensity and increase in peak intensity are similar to our observation, however, the thickness range they have studied ranges

55nm to 210nm. The dipole method simulation based on transfer matrix formalism predicts their observation. The study suggests extensive simulation is required to predict observed effect.

6.4 Conclusion

In conclusion, we observe thickness dependent luminescence shift in a widely used organic material. We show a good correlation between the blue shift and intrinsic scaling property by calculating fractal dimension of the surface. Using phase contract atomic force microscopy we have shown clear formation of nanovoids and grain growth. Further study in terns of interface and transient electroluminescence can help explain some of the observations.

CHAPTER 7. Organic Light Emitting Diode with Short Reduction Layer*

7.1 Introduction

Organic materials continue to attract scientific and technological interest due to its easy applicability to fabricate light emitting diodes and large area flexible display with wide range of advantages like fast response time, low power consumption and structural simplicity [105-107]. With continued improvement in material and process the improvements are showing feasibility for panel lighting. However, a wide range of fundamental issues needs to be addressed in order to optimize any device structure. From a materials point of view, formation and transport of spin and singlet and triplet excited states and effect of surface/interface morphology remains a strong focus [108].From high volume manufacturing point of view, the "yield" of the OLED device i.e. the number of good pixels to the number of dead pixels is a important parameter that needs to be significantly improved. Tyan et al [109] has discussed the causes for low yields and possible solution to address the issue. The problem and the solution discussed in Ref 109, is mentioned below. Typical OLED devices consist of layers of organic thin films sandwiched between an anode and cathode. Typically, the organic layers are about 100nm to 200nm in thickness and the voltage applied between the electrodes is about 3 to 10V. Because of the small separation, the electric field across the organics is very high

and the OLED is prone to “shorting defects”. Pinholes, cracks, defects, steps in the structure of the OLED devices and roughness of the substrates etc can cause shorts i.e. direct contact between the anode and the cathode which can result in dead pixels or reduced luminous output of the OLED device. In a multi-pixel display device, the shorting defects could result in dead pixels that do not emit light or emit below average intensity of light causing reduced display quality. In lighting or other low resolution applications, the shorting defects could result in a significant fraction of area non-functional. Because of the concerns on shorting defects, the fabrication of OLED devices is typically done in clean rooms. But even a clean environment cannot be effective in eliminating the shorting defects. In many cases the thickness of the organic layers is also increased to beyond what is actually needed for functioning devices in order to increase the separation between the two electrodes to reduce the number of shorting defects. These approaches add costs to OLED device manufacturing, and even with these approaches the shorting defects cannot be totally eliminated. The shorting defects are particularly problematic for large area devices. Because the most random defects f follow Poisson distribution, the yield of the defect free devices drops exponentially with increased device surface area. Ref 147 outlined an elegant method to reduce the detrimental effects of the shorting defects. Figure 7.1 is a schematic diagram of a shorting defect in an OLED device.

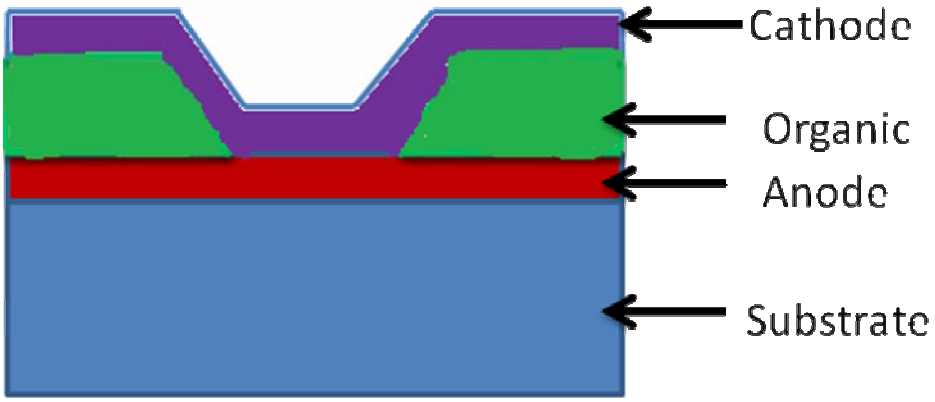

Figure 7.1 Schematic diagram of a shorting defect in an OLED Device

Here the shorting defect can be formed by dust particles or flakes on the substrate. The particles or flakes that are present on the substrate during organic deposition process and subsequently fall off can cause the most damage. They block the organic materials from depositing onto the substrate and when they fall off, they leave an area of the first electrode layer completely exposed to the latter deposition of the second electrode layer. Other sources of shorting defects include steps in the OLED device structure. In addition, rough textures on the surface of the substrate or the surface of the first electrode layer could also induce shorting defects. In all cases, when a current is applied to operate the OLED, a path of least resistance is provided by the shorting defects, resulting in all the current passing through the defect and the device performance is reduced significantly. Carrying out the device fabrication process in a clean room environment is a primary method to reduce shorts. There is a limit, however one possible solution suggested [109] is to increase the thickness of the organic layers to reduce the shorting defects. This would not only increase the material and process costs, but it would also increase the device voltage as well, which is not desirable. Tyan et al proposed a

generally effective method to reduce shorting defects. Figure 7.2 is a schematic diagram of the OLED device with the shorting defect and the short reduction layer as proposed by Tyan et al.

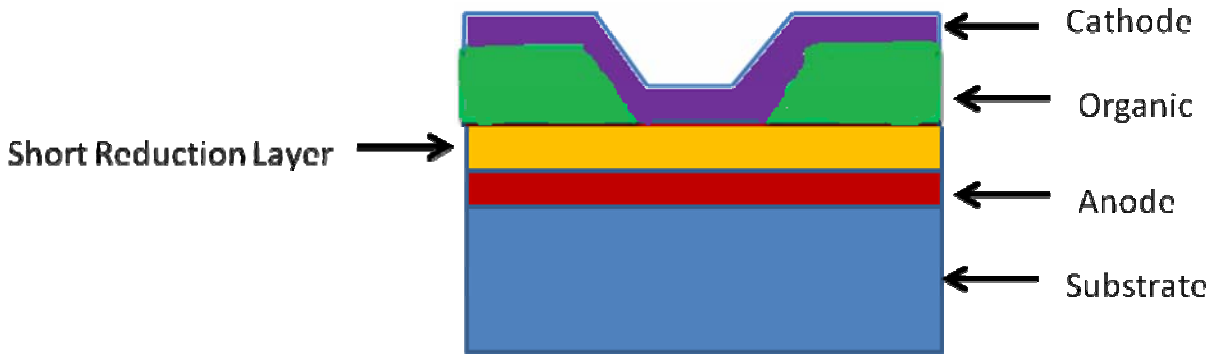

Figure 7.2 Schematic diagram of OLED with SRL layer

In this method a thin transparent layer, the short reduction layer (SRL) having appropriate electrical resistivity between the two electrodes is deposited. Because the area of the shorting defect is much smaller than the area of the device, the SRL adds an electrical resistance to the shorting defect that is much higher than the one it adds to the device. As a result, the applied current flows through the device instead of the defects. Hence the shorting defects no longer adversely affect the operation and efficiency of the OLED. A more detailed description of the usefulness of the SRL layer and the properties of the SRL layer are described in the following passages.

Figure 7.3 is a schematic diagram of the device with a SRL layer deposited between the anode and the organic layer.

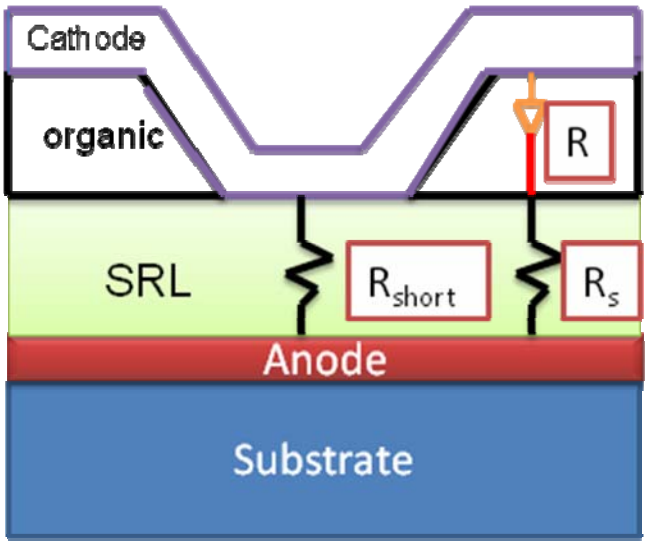

Fig 7.3: Schematic diagram of the device with a SRL layer deposited between the anode and the organic layer.

When the SRL layer is deposited as shown in the Fig8.3, the top electrode is not in direct contact with the bottom electrode through the short defect or pinhole, but via the short reduction layer. Under operating conditions, the device without the SRL layer has an effective resistance R given by $R= V_d/ (I_d. A_d)$ where Ad is the total device area, Id is the operating current density, V_d is the operating voltage of the device .The SRL layer adds a series resistance Rshort to the pinhole and a resistance R_s to the device itself. The applied current does not flow through the pinhole or the shorting defect if $R_{short} >> R+ R_s$ and the shorting defect will no longer affect the operation of the OLED device. The condition $R_{short} >> R +R_s$ can be easily achieved since in most practical cases $A_d >> A_{short}$, where A_{short} is the area of the defect.

The typical thickness of the OLED devices is about 100 to 300nm and the layer thickness is optically tuned to optimize the emission efficiency of the device. As SRL

becomes a part of the optical structure of the device, its preferred thickness range is from about 20nm to about 200nm and the effectiveness of the SRL layer depends on the area ratio between the device and the shorting defects. The SRL layer needs to be thick enough to effectively cover the shorting defects and hence the technique used to deposit the SRL layer should enable deposition of a uniform, conformal layer.

Important thing to note is that the effectiveness of the SRL layer is dependent on the area ratio between the device and the shorting defect. For large area OLED devices such as Solid state lighting, area ratio is very large and the difference in the resistance values of the short reduction layer adds to the device and to the shorting defects, which can be large.

7.2 SRL Deposition

One of the potential materials of interest for SRL is ZnO (Zinc Oxide). The deposition method used for deposition of the SRL layer is very critical. It is well known that thermal evaporation and e beam evaporation do not produce uniform and conformal thin films. Sputtering deposition does produce conformal thin films, but can result is sputter damage which can increase the number of shorting defects which is counterproductive to the purpose of reducing shorts. Atomic layer deposition is a popular deposition technique which has been in use in recent times for its ease of operation and also the films deposited using ALD are very uniform, conformal and ideal for depositing ZnO film as SRL. The working principle and other details of the ALD system can be understood from

the references mentioned here. For the deposition of ZnO using ALD, Dimethyl Zinc was used as the precursor. Fig 7.4 shows the deposition cycle for ZnO using ALD.

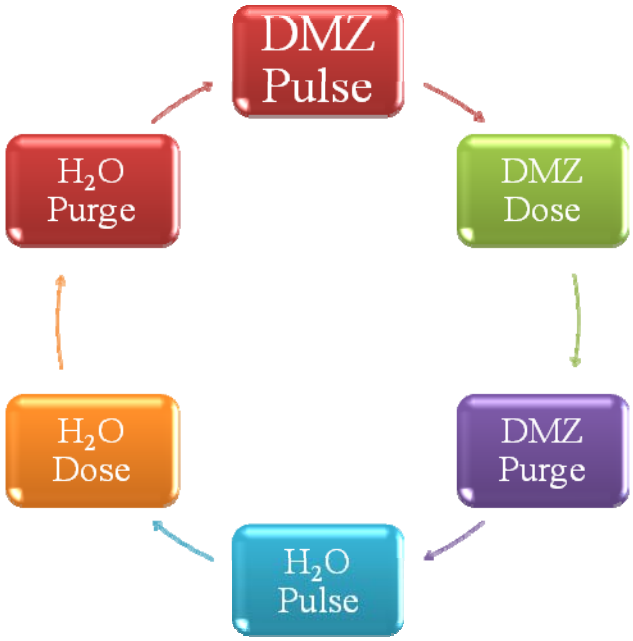

Fig7.4: Schematic diagram showing the ALD process for deposition of ZnO

Initially, the DMZ valve is open for a certain amount of time and then closed. Then the DMZ enters the chamber and allowed to react with hydroxyl groups on the surface of the substrate to form Zn with methyl dangling bonds. The reaction is continued till the surface is passivated .As DMZ does not react with itself, the reaction is terminated to one layer. Methane is the by product. Next, the excess DMZ and methane is purged from the chamber using nitrogen. Next water vapor is sent into the chamber which reacts with the methyl dangling bonds forming Zn-O bridges with hydroxyl groups on the surface. The excess methane is again purged using nitrogen gas. This cycle is repeated number of times till the required thickness of the film is obtained. Importantly, for obtaining a

conformal, uniform film, DMZ pulse, DMZ dose, H_2O pulse and H_2O dose need to be optimized.

7.3 Analytical Study of SRL thin film

Various analytical tools were used to understand the properties of ZnO. This section briefly talks about those analytical results.

i) AFM Analysis: Figure 7.5 is topolographical and phase image of the ZnO grown using ALD. The topographical image shows that the film is uniform. The phase image shows the soft and hard regions on the film and also indicates that there is no contamination of the film.

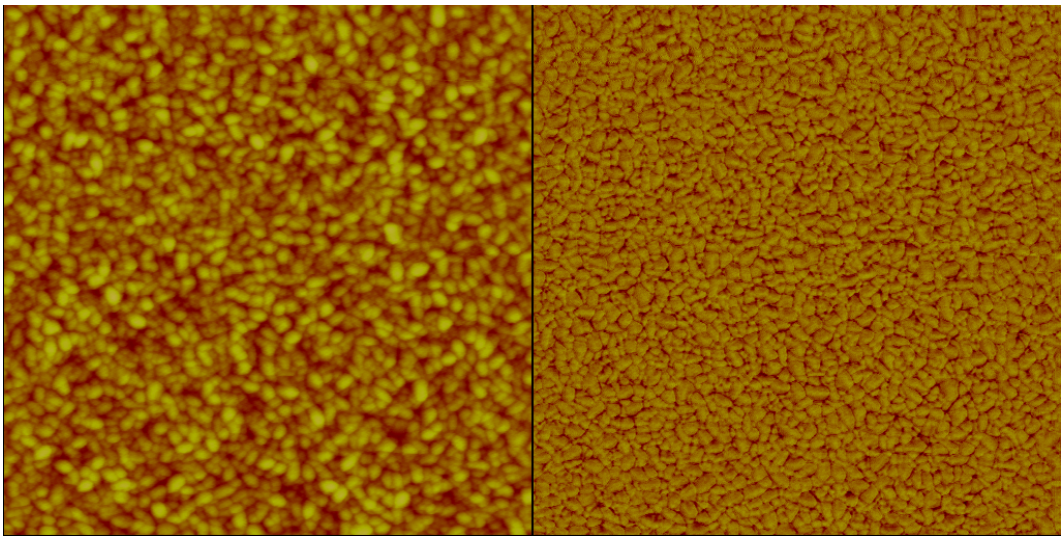

Figure 7.5 Topolographical and phase image of the ZnO grown using ALD

ii) **XPS Analysis**: XPS data shows the elemental composition of the ZnO film. It contains 62% of zinc, 35% of oxygen and 3% of carbon.

iii) XRD Analysis: Figure 7.6 is the XRD of ZnO film. It can be seen that ZnO is polycrystalline in nature.

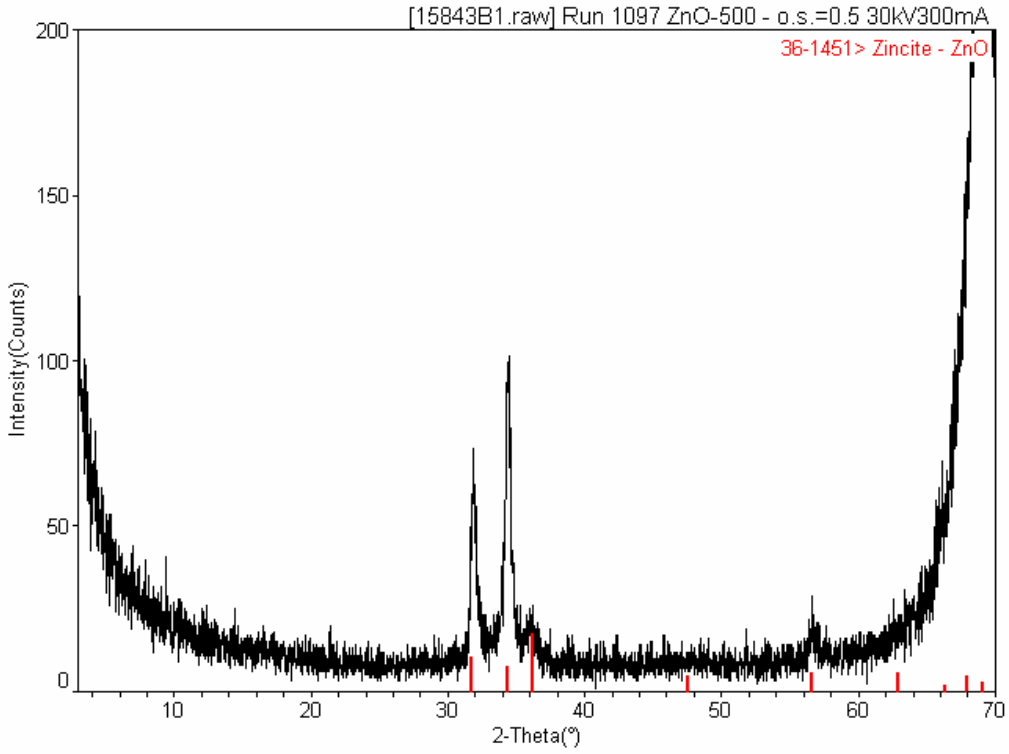

Figure 7.6 XRD image of ZnO film grown using ALD.

7.4 ZnO performance as a SRL

I-V curves for OLED device were fabricated without ZnO as SRL and with ZnO as SRL are shown in Fig 7.7 and Fig7. 8. The device without ZnO had about 95% shots. Using ZnO as SRL, OLED device had only 1.4% shots, meaning 98% improvement was seen in the OLED device with ZnO SRL.

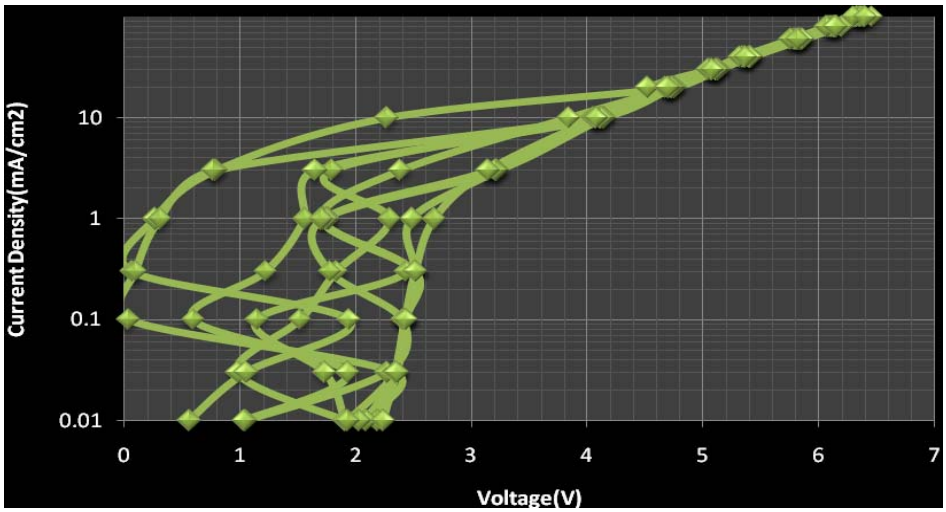

Figure 7.7 I-V curves of OLED devices without ZnO SRL.

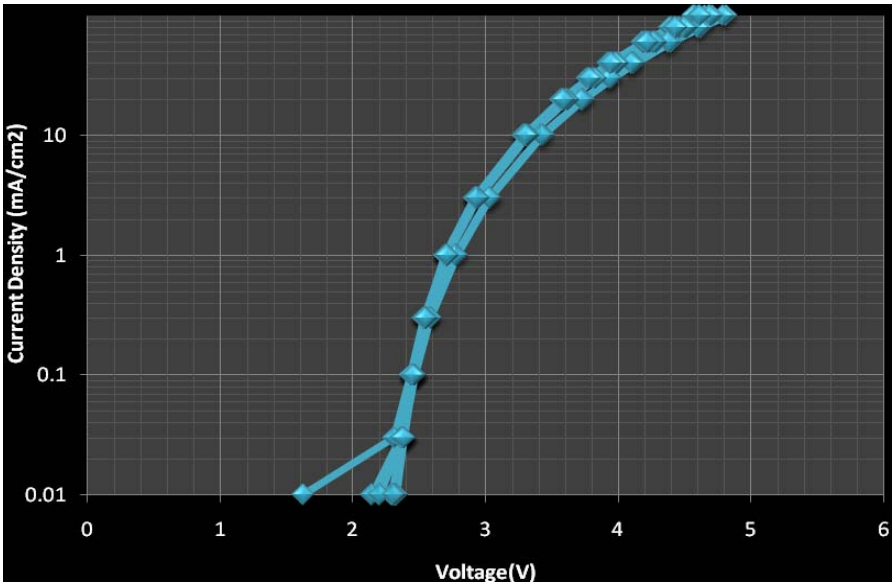

Figure 7.8: I-V curves for OLED with ZnO SRL.

7.5 Conclusions

Using ZnO as Short reduction layer, 98% improvement has been be achieved in the OLED devices when compared to the OLED without the ZnO SRL layer.

* This work is done a part of the co op at Eastman Kodak Company.

Bibliography

[1] Bhargava Kanchibotla, "Magnetic Properties of Iron Nanostructures," Master's thesis, 2005.

[2] S. Bandyopadhyay, "Quantum Information Science from the Perspective of a Device and Materials Engineer," Advanced Semiconductor and Organic Nanotechniques, Part 1, Ed. H. Morkoc (Elsevier, USA, 2003), Chapter 9.

[3] B. Kanchibotla, S. Pramanik and S. Bandyopadhyay, "Self-assembly of nanostructures using nanoporous alumina templates," Chapter 9 in Nano and Molecular Electronics HandbookEd. S. Lyshevski, CRC press (Taylor and Francis), 2007.

[4] J. P. O'Sullivan and G. C. Wood," The morphology and mechanism of formation of porous anodic films on aluminum" Proc. R. Soc. London, Ser. A, 1970,317,511.

[5] V. P. Parkhutik and V. I. Shershulsky, " Theoretical modelling of porous oxide", J. Phys. D: Appl. Phys. 25,1258.

[6] Jessensky,O. et al., Self-organized formation of hexagonal pore arrays in anodic alumina, Appl. Phys .Lett., 72, 1173,1998.

[7] Li, A.P. et al., Polycrystalline and monocrystalline pore arrays with large interpore distance in anodic alumina, Electrochem Solid-State Lett., 3, 131, 2000.

[8] Ono, S., et al., Self-ordering of anodic porous alumina formed in organic acid electrolytes, Electrochimica Acta., 51, 82, 2005.

[9] Palibroda, E., Aluminum porous oxide growth—II. On the rate determining step, Electrochim. Acta., 40, 1051 ,1995

[10] Almawlawi, D. et al., Magnetic properties of Fe deposited into anodic aluminum oxide pores as a function of particle size, *J. Appl. Phys.*, 70, 4421, 1991.

[11] Li,W.S. et al., Influence of anodizing conditions on the ordered pore formation in anodic alumina, *J Phys D: Appl Phys.*, 33, 2527, 2000.

[12] Masuda, H. and Fukuda, K., Ordered metal nanohole arrays made by a two-step replication of honeycomb structures of anodic alumina, *Science*, 268, 1466, 1995.

[13] Ansermet, J.P et al., Bridging the gap between template synthesis and microelectronics: spin-valves and multilayers in self-organized anodized aluminium nanopores, *Nanotechnology*, 14, 978, 2004.

[14] S. Pramanik, C.-G. Stefanita, S. Patibandla, S. Bandyopadhyay, K. Garre, N. Harth, and M. Cahay, Nat. Nanotechnol. **2**, 216 (2007).

[15] G. Salis, S. F. Alvarado, M. Tschudy, T. Brunschwiler, and R. Allenspach, Phys. Rev. B **70**, 085203 (2004)

[16] S. Bandyopadhyay, B. Das, and A. E. Miller, Nanotechnology **5**, 113 (1994).

[17] S. Bandyopadhyay, Superlattices Microstruct. **37**, 77 (2005).

[18] S. Bandyopadhyay, Superlattices Microstruct. **22**, 411 (1997).

[19] D. Loss and D. P. DiVincenzo, Phys. Rev. A **57**, 120 (1998).

[20] B. E. Kane, Nature (London) **393**, 133 (1998)

[21] S. Bandyopadhyay, Phys. Rev. B **61**, 13813 (2000).

[22] T. Calarco, A. Datta, P. Fedichev, E. Pazy, and P. Zoller, Phys. Rev. A **68**, 012310 (2003).

[23] A. E. Popescu and R. Ionicioiu, Phys. Rev. B **69**, 245422 (2004).

[24] E. Knill, Nature (London) **434**, 39 (2005).

[25] J. Lehmann, A. Arino-Gaita, E. Coronado, and D. Loss, Nat. Nanotechnol. **2**, 312 (2007).

[26] R. de Sousa and S. Das Sarma, Phys. Rev. B **67**, 033301 (2003).

[27] X. Hu, R. de Sousa, and S. Das Sarma, in Foundations of Quantum Mechanics in the Light of New Technology, edited by Y. A. Ono and K. Fujikawa (World Scientific, Singapore, 2003).

[28] S. Sanvito, Nature Mater. **6**, 803 (2007).

[29] G. S. Huang, X. L. Wu, Y. Xie, F. Kong, Z. Y. Zhang, G. G. Siu, and P. K. Chu, Appl. Phys. Lett. **87**, 151910 (2005), and references therein.

[30] S. Bandyopadhyay, A. E. Miller, H.-C. Chang, G. Banerjee, V. Yuzhakov, D.-F. Yue, R. E. Ricker, S. Jones, J. A. Eastman, E. Baugher, and M. Chandrasekhar, Nanotechnology **7**, 360 (1996).

[31] H. Masuda and M. Satoh, Jpn. J. Appl. Phys., Part 2 **35**, L126 (1996).

[32] D. D. Macdonald, J. Electrochem. Soc. **140**, L27 (1993).

[33] S. Ono, H. Ichinose, and N. Masuko, J. Electrochem. Soc. **138**, 3705 (1991)

[34] M. N. Grecu, A. Mirea, C. Ghica, M. Colle, and M. Schwoerer, J. Phys.: Condens. Matter **17**, 6271 (2005), and references therein.

[35] P. H. Rieger, *Electron Spin Resonance: Analysis and Interpretation* (The Royal Society of Chemistry, Cambridge, 2007).

[36] Y. Du, W. L. Cai, C. M. Mo, J. Chen, L. D. Zhang, and X. G. Zhu, Appl. Phys. Lett. **74**, 2951 (1999).

[37] H. Benisty, C. M. Sotomayor-Torres, and C. Weisbuch, Phys. Rev. B **44**, 10945 (1991).

[38] A. Akhkalkatsi, T. Gegechkori, G. Mamniashvili, Z. Shermadini, A. N. Pogorely, and O. M. Kuzmak, arXiv:0705.3979 (unpublished).

[39] T. A. Kennedy, J. S. Colton, J. E. Butler, R. C. Linares, and P. J. Doering, Appl. Phys. Lett. **83**, 4190 (2003).

[40] J. Wrachtrup, S. Ya. Kilin, and A. P. Nizovtsev, Opt. Spectrosc. **91**, 429 (2001).

[41] M. V. G. Dutt, L. Childress, L. Jiang, E. Togan, J. Maze, F. Jelezko, A. S. Zibrov, P. R. Hemmer, and M. D. Lukin, Science **316**, 1312 (2007).

[42] M. S. Shahriar, J. A. Bowers, G. Demsky, P. S. Bhatia, S. Lloyd, P. R. Hemmer, and A. E. Craig, Opt. Commun. **195**, 411 (2001).

[43] S. Ghosh, V. Shi, W. H. Lau, D. D. Awschalom, S. Y. Bae, S. Wang, S. Vaidya, and G. Chapline, Appl. Phys. Lett. **86**, 232507 (2005).

[44] S. Gustavsson, M. Studer, R. Leturcq, T. Ihn, K. Ensslin, D. C. Driscoll, and A. C. Gossard, Phys. Rev. Lett. **99**, 206804 (2007).

[45] Bandyopadhyay, S., et al., Electrochemically assembled quasi periodic quantum dot arrays. *Nanotechnology*. **7,** 360-371 (1996).

[46] Rabin, O., Herz, P. R., Cronin, S. B., Lin, Y-M, Akinwande, A. I. & Dresselhaus, M. Mat. Res. Soc. Symp., **636**, D.4.7.1. (2001).

[47] Lakowicz, J. R., Shen, Y., Gryczynski, J., D'Auria, S. & Gryczynski, I. Intrinsic fluorescence from DNA can be enhanced by metal particles. *Biochem. Biophys. Res. Commun*., **286**, 875 (2001).

[48] Lakowicz, J. R. Radiative decay engineering: Biophysical and biomedical applications. *Anal. Biochem.*, **298**, 1 (2001).

[49] Aslan, K., Gryczynski, I., Malicka, J., Matveeva, E., Lakowicz, J. R. & Geddes, C. D. Metal enhanced fluorescence: An emerging tool in biotechnology. *Curr. Opin. Biotechnol.*, **16**, 55 (2005).

[50] Ray, K., Badugu, R. & Lakowicz, J. R. Metal enhanced fluorescence from CdS nanocrystals: A single molecule fluorescence study. *J. Am. Chem. Soc*. **128**, 8998 (2006).

[51] Wang, Z., Chen, Z., Lan, Z., Zhai, X., Du, W. & Gong, Q. *Appl. Phys. Lett.,* **90**, 151119 (2007).

[52] Cohen-Tannoudji, C., Diu, B. & Laloe, F. *Quantum Mechanics,* Vol. 2 (Wiley, New York, 1977).

[53] Premvardhan, L., Wachsmann-Hogiu, S., Peteaunu, L. A., Yaron, D. J., Wang, P-C., Wang, W. & McDiarmid, A. J. Conformational effects on optical charge transfer in the emeraldine base form of polyaniline from electroabsorption measurements and semiempirical calculations. *J. Chem. Phys*., **115**, 4359 (2001).

[54] W Lee, K Nielsch and U Gösele, Nanotechnology, 18, 475713 (2007)

[55] Andrew J. Rahedi, Jack F. Douglas, and Francis W. Starr , J. Chem. Phys. 128, 024902 (2008)

[56] Cameron Keenan, Sandeep Chandril, Thomas H. Myers, David Lederman, E.

Ramos-Moore, and A. L. Cabrera , Appl. Phys. Lett. 92, 013119 (2008)

[57] P. Hancock and R. C. Hurst, in Advances in Corrosion Science and Technology, edited by R. W. Staehle and M. G. Fontana (Plenum, New York, 1974)

[58] P. E. Doherty and R. S. Davis, J. Appl. Phys. 34, 619 (1963)

[59] A. G. Reversz and F. P. Fehlner, Oxid. Met. 15, 297 (1981)

[60] F. P. Fehlner, Low-Temperature Oxidation: the Role of Vitreous Oxides (Wiley-Interscience, New York, 1981).

[61] K. R. Lawless, Rep. Prog. Phys. 37, 231 (1973)

[62] C. E. Aumann, G. L. Skofronick, and J. A. Martin, J. Vac. Sci. Technol. B 13, 1178 (1995).

[63] Guangwen Zhou, William S. Slaughter, and Judith C. Yang ,Phys. Rev. Lett. 94, 246101 (2005)

[64] Hiroo Omi, Hiroyuki Kageshima, and Masashi Uematsu ,Phys. Rev. Lett. 97, 016102 (2006)

[65] H. Masuda and K. Fukuda, Science 268, 1466 (1995)

[66] K Watanabe, Y Takemura, Y Shimazu and J Shirakashi,Nanotechnology 15, S566 (2004)

[67] G. J. Ackland, Phys. Rev. E **66**, 041605 (2002), B. D. Krack, V. Ozoli, M. Asta, and I. Daruka, Phys. Rev. Lett. **88**, 186101 (2002),P. Bak, R. Bruinsma, Phys. Rev. Lett. Phys. Rev. Lett. 49, 249 - 251 (1982), B. Mandelbrot, Fractals: Form, Chance, and Dimension (Freeman, San Fransisco, 1977)

[68] D. Aurongzeb, E. Washington, M. Basavaraj, J. M. Berg, H. Temkin, and M. Holtz ,J. Appl. Phys. 100, 114320 (2006)

[69] D. Aurongzeb, K. Bhargava Ram, M. Holtz, M. Basavaraj, G. Kipshidze, B. Yavich, S. A. Nikishin, and H. Temkin ,J. Appl. Phys. 99, 014308 (2006)

[70] D. Aurongzeb, Applied surface science, 252,872(2005)

[71] L. Goluvobic and R. Bruinsma, Phys. Rev. Lett.60,321(1991)

[72] J.C. Yang,B. Kolasa, J. Gibson and M Yeadon, App. Phys. Lett.,73,2841(1998)

[73] L. P. H. Jeurgens, W. G. Sloof, F. D. Tichelaar, and E. J. Mittemeijer ,Phys. Rev. B 62, 4707 (2000)

[74] P. E. Doherty and R. S. Davis, J. Appl. Phys. 34, 619 (1963)

[75] S. Das Sarma, S. V. Ghaisas, and J. M. Kim, Phys. Rev. E 49, 122 (1994)

[76] M. López, M. A. Rodríguez, and R. Cuerno, Physica (Amsterdam) 246A, 329 (1997)

[77] J. M. López, M. Castro, and R. Gallego, Phys. Rev. Lett. 94, 166103 (2005).

[78] S. Das Sarma and S. V. Ghaisas, Phys. Rev. Lett. 69, 3762 (1992); 71, 2510 (1993)

[79] P. Meakin, Phys. Rev. Lett. 51,1119(1983)

[80] M. H Junji Tominaga, J. Phys.: Condens. Matter 15, R1101 , (2003)

[81] Rajesh V Nair and R Vijaya, J. Phys. D: Appl. Phys. 40, 990, (2007)

[82] Byeong-Joo Lee, Jae-Hyeok Shim, and M. I. Baskes ,Phys. Rev. B 68, 144112 (2003)

[83] J. H. Burroughes, D. D. C. Bradley, A. R. Brown, R. N. Marks, K. Mackay, R. H. Friend, P. L. Burn, and A. B. Holmes, Nature (London) 347, 539 (1990).

[84] M. A. Baldo, S. Lamansky, P. E. Burrows, M. E. Thompson, and S. R. Forrest, Appl. Phys. Lett. 75, 4 (1999)

[85] Jun-ho Choi, Kyung-Ho Kim, Se-Jin Choi and Hong H Lee, Nanotechnology , 9, 2246 (2006)

[86] .E. L. Williams, K. Haavisto, J. Li, G. E. Jabbour, Advanced Materials,19,197(2007)

[87] O. D. Gordan, C. Himcinschi, D. R. T. Zahn, C. Cobet, N. Esser, and W. Braun Appl. Phys. Lett. 88, 141913 (2006)

[88] M. Castellani and D. Berner ,J. Appl. Phys. 102, 024509 (2007)

[89] M. M. Levichkova, J. J. Assa, H. Fröb, and K. Leo, Appl. Phys. Lett. 88, 201912 (2006)

[90] Le-Le Li, Chen-Jie Fang, Quan Yuan, and Chun-Hua Yan ,Appl. Phys. Lett. 90, 231908 (2007)

[91] Norifumi Kajimoto, Takaaki Manaka, and Mitsumasa Iwamoto ,J. Appl. Phys. 100, 053707 (2006)

[92] M S Xu, J B Xu, H Z Chen and M Wang, J. Phys. D: Appl. Phys., 18, 2618(2004)

[93] A. J. Drew et al., Phys. Rev. Lett. 100, 116601 (2008)

[94] B. Xu, L. Chen, X. Liu, H. Zhou, H. Xu, X. Fang, and Y. Wang , Appl. Phys. Lett. 92, 103305 (2008)

[95] L. F. Cheng, L. S. Liao, W. Y. Lai, X. H. Sun, N. B. Wong, C. S. Lee, and S. T. Lee, Chem. Phys. Lett. 319, 418 (2000)

[96] S. Caria, E. Da. Como, M. Murgia, R. Zamboni, P. Melpignano, and V. Biondo, J. Phys.: Conds. Mat. 18, S2139 (2006).

[97] A. Curioni, M. Boreo, and W. Andreoni, Chem. Phys. Lett. 294, 263 (1998).

[98] A. Curioni, W. Andreoni, R. Treusch, F. J. Himpsel, E. Haskal, P. Seidler, C. Heske, S. Kakar, T. van Buuren, and L. J. Terminello, Appl. Phys. Lett. 72, 1575 (1998)

[99] M. Braun, J. Gmeiner, M. Tzolov, M. Coelle, F. D. Meyer, W. Milius, H. Hillebrecht, O. Wendland, J. U. von Schütz, and W. Brütting, J. Chem. Phys. 114, 9625 (2001)

[100] J. M. Leger, S. A. Carter, B. Ruhstaller, H.-G. Nothofer, U. Scherf, H. Tillman, and H.-H. Hörhold , Phys. Rev. B 68, 054209 (2003)

[101] Philip Draviam, M.S. Thesis, University of Cincinnati (2005)

[103] H. E. Stanley, in Fractals and Disordered Systems, edited by A. Bunde and S. Havlin (Springer-Verlag, Berlin,1991)

[104] Felipe Barra, Benny Davidovitch, Anders Levermann, and Itamar Procaccia, Phys. Rev. Lett. 87, 134501 (2001)

[105] C. W. Tang, S. A. VanSlyke, Appl. Phys. Lett. 1987, **51**, 913.

[106] M. A. Baldo, S. Lamansky, P. E. Burrows, M. E. Thompson, and S. R. Forrest, Appl. Phys. Lett. 75, 4 (1999)

[107] M. Castellani and D. Berner, J. Appl. Phys. 102, 024509 (2007).

[108] M. M. Levichkova, J. J. Assa, H. Fröb, and K. Leo, Appl. Phys. Lett. 88, 201912 (2006)

[109] Yuan-Sheng Tyan, Giuseppe Farruggia, and Thomas R. Cushman, SID Digest 2007

Short Vita of Bhargava Kanchibotla

Education

- **Doctor of Philosophy, Electrical Engineering** **August 2009**
  Virginia Commonwealth University, USA
- **Master of Science, Physics** **May,2005**
  Texas Tech University, USA
- **Master of Science, Electronics** **May, 2001**
  University of Hyderabad, India
- **Bachelor of Science, Electronics** **May, 1999**
  Osmania University, India

Publications

- Peer Review Journal Papers : 12 (including under review and published)
- Conference Proceedings : 10
- Book Chapters: 3

Professional Affiliations

- Student Member- IEEE, APS, MRS,SPIE,AAAS